Development of medical devices for diagnosing cartilage injury and metastatic cancers

by

Yi-Hui Huang

Presented to the Faculty of the Graduate School of

The University of Texas at Arlington in Partial Fulfillment

of the Requirements

for the Degree of

DOCTOR OF PHILOSOPHY IN BIOMEDICAL ENGINEERING

The University of Texas at Arlington

August 2019

ACKNOWLEDGEMENTS

I want to say thank you to my parents and Dr. Wen S. Chan from the MAE department and his wife for their support. Because of them, I am enthusiastic about my research. I also want to thank my PI, Dr. Liping Tang. His constructive critiques helped me develop better experimental methods to solve the problems in my study. And finally, thank you to all the collaborators and lab members with whom I have worked over these years.

Collaborators

- Dr. Harry K. W. Kim, Dr. Matthew C. Phipps, Dr. Joseph Borrelli, Dr. Jer-Tsong Hsieh, Dr. Ramesh Saxena, Dr. Zui Pan, Dr. Yi Hong, Dr. Yan Chang, Dr. Cancan Xu, and Dr. Jinglei Wu

Lab members

- Dr. Jun Zhou, Dr. Hong Weng, Dr. Ashwin Nair, Dr. Wei Cong, Dr. Ashley Dacy, Dr. MinKyung Khang, Mr. Amir Hakamivala, Mr. Shuxin Li, Ms. Joyita Roy, Ms. Tanmayee Chikate, Ms. Jacqueline Fu, Mrs. Kayti Ashton Robinson, Mr. Ali Mohamedi, Mr. Carlos Cantu and Mr. Chuka Okpokwasili

August 2019

Abstract

Development of a medical device for diagnosing cartilage injury and metastatic cancers

The University of Texas at Arlington, 2019

Supervising professor: Dr. Liping Tang

My research focused on applying biomedical engineering techniques to diagnose different diseases and conditions. The results of these work led to one published paper and two submitted manuscripts which are summarized in Chapters 2, 3 &4.

Briefly, in Chapter 2, my work laid emphasis on developing a method for early detection of cartilage injury. An apoptotic cell-detecting probe was fabricated by the conjugation of the apoptotic cell-binding peptide (CQRPPR) and a sulfo-cyanine7 N-hydroxysuccinimide ester (Cy7 dye). Both *in vitro* and *ex vivo* examination showed an excellent relationship between the number of apoptotic chondrocytes and probe binding affinity. Finally, using a xiphoid injury model was created using mechanical pressure, we found that the apoptosis probes may serve as a powerful tool to monitor the extent of mechanical force-induced cartilage injury *in vivo*.

In Chapter 3, my work was centered on the creation and optimization of a new device, "cancer trap", for capturing migrating prostate cancer (PCa) cells. The cancer trap is composed of hyaluronic acid microparticles that have good cell and tissue compatibility and can extend the release of chemokines to 4 days *in vitro*. After testing various chemokines, Erythropoietin (EPO) and stromal-derived factor-1α (SDF1α) are the best chemokines for chemokine-releasing cancer

traps *in vitro*. Finally, using an intravenous PCa transplantation model, we found that subcutaneously implanted and EPO- releasing cancer trap attracted many circulating PCa and significantly reduced cancer spreading in the lung. These results support that cancer traps may serve as a unique device to sequester circulating PCa cells and subsequently reduce distant metastasis.

In Chapter 4, we expanded the use of cancer capturing devices from cancer trapping devices to cancer diagnosis devices. For that, our study focused on metastatic esophageal cancer (EC). EC lymph node (LN) metastasis is one of the most important prognostic factors and the inability to diagnose EC earlier is believed to be responsible for the poor prognosis. To overcome such a challenge, my study was aimed at engineering an implantable device, a "diagnostic trap, ", capable of intercepting migrating ECs prior to LN metastasis for early EC diagnosis. A diagnosis cancer trap was composed of a biocompatible Gelfoam and EPO. The results of our orthotopic EC animal study demonstrated that diagnostic trap recruited $4.03x10^4$ migrating cancer cells. The diagnostic trap not only recruited $EGFR^+$ cancer cells but also decreased LN metastasis. Histological analysis proved that the porous structure increased the capacity of the cancer trap to allow more cancer cell infiltration compared to the previous design. The overall results support that trap implants can be used for diagnosing EC metastasis and, potentially, for reducing LN metastasis.

Table of Contents

List of Figures

Chapter 1. Introduction

My thesis is composed of a series of studies which are focused on the development of a new diagnosis and treatment tools for cartilage injury and cancers using biomedical engineering technique. While the pathological processes governing injured cartilage and metastasis cancers are very different, I was able to create new methodologies for diagnosing and treating such diseases based on existing biomedical engineering methodologies and techniques. The results of these work are summarized in the following chapters (Chapter 2, 3, &4).

In Chapter 2, our goal was to develop a new diagnostic tool for injured cartilage. Cartilage injury induced by acute excessive contact stress is common and mostly affects a young adult. The common symptoms of the injured cartilages are joint pain and stiffness, reduced mobility and function. These patients also suffered from poor quality of life and increased lifetime medical costs. The conventional diagnostic methods are a physical examination, radiograph of the joint, synovial fluid tests, computed tomography scans and magnetic resonance imaging. Although early detection of cartilage injury may prevent serious and lifelong arthritic complications, early detection and treatment are not possible due to the lack of a reliable detection method. To solve the challenge, an apoptotic cell-detecting probe was fabricated by the conjugation of an apoptotic cell-binding peptide (CQRPPR) and a sulfo-cyanine7 N-hydroxysuccinimide ester (Cy7 dye). After the *in vitro* biocompatibility test, *in vitro* and *ex vivo* examination have shown the high correlation between the number of apoptotic chondrocytes and probe binding affinity. A xiphoid injury model was created using mechanical pressure. After the injection of the apoptotic cell-detecting probe, the healing procedure of early injury on the xiphoid was observed for 7 days. The results support that

the apoptosis probes may serve as a powerful tool to monitor the extent of mechanical force-induced cartilage injury *in vivo*.

In Chapter 3, my work was focused on fabricating and optimizing an implantable device, "cancer trap", for treating metastatic prostate cancer (PCa). PCa is the most prevalent cancer in U.S. men and many other countries. The current medical tests include prostate-specific antigen (PSA) test, transrectal ultrasound, and prostate biopsy test. For the late stage of PCa, the treatments are radiation, chemotherapy, surgery, and hormone therapy. The survival rate of EC patients drops from 100% to 28% after distant metastasis occurs. It becomes more difficult and inefficient to treat patients after cancer spreading. Although primary PCa can be controlled with surgery or radiation, treatment options of preventing metastatic PCa are still limited. An alternative treatment was designed to capture migrating cancer cells from the bloodstream. The cancer trap is composed of hyaluronic acid microparticles that have good cell and tissue compatibility and can extend the release of chemokines to 4 days *in vitro*. After testing various chemokines, Erythropoietin (EPO) and stromal derived factor-1α (SDF1α) are the best chemokines for chemokine-releasing cancer traps *in vitro*. The animal study showed that cancer trap attracted many circulating PCa among the rest and significantly reduced cancer spreading in the lung after IV injection of cancer cells. These results support that cancer trap may serve as a unique device to sequester circulating PCa cells and subsequently reduce distant metastasis.

In Chapter 4, the cancer trap device was modified as "diagnosis trap" for diagnosing esophageal cancer (EC). EC patients often have lower 5-year survival rate when cancer progression starts from the localized tumor (45%) to regional lymph node metastasis (24%) or distant metastasis (5%). The earlier treatments provide better outcomes for esophageal cancer patients. The routine diagnostic tests are esophagram, endoscopy, endoscopic ultrasound, CT, MRI, PET, bronchoscopy

and biopsy tests. For EC patients, there are several treatments such as surgery, chemotherapy, radiation therapy and endoscopic treatments. However, the inability to diagnose EC earlier is believed to be responsible for the poor prognosis. To overcome such a challenge, this study was aimed at engineering an implantable diagnosis trap capable of capturing spreading ECs prior to LN metastasis for early EC diagnosis. Based on our previous study, we selected EPO after several tests on migration assays. In order to isolate cancer cells, the material criteria of the diagnosis trap should be implantable, biocompatible, retrievable and suitable for cell recovery. Because HA particles are neither retrievable nor suitable for cell recovery, Gelfoam is chosen as the base of the diagnosis trap. A diagnosis trap was composed by a biocompatible Gelfoam and EPO. KYSE-30 (a highly metastatic cancer line) and KYSE-70 (a poorly metastatic cancer line) were used as model cell lines to examine the efficacy of cancer trap. Our orthotopic EC animal study demonstrated that diagnostic cancer trap recruited $4.03x10^4$ migrating cancer cells. A diagnostic cancer trap not only recruited $EGFR^+$ cancer cells but also decreased LN metastasis. Compared with two different cancer cell lines, the diagnostic trap can differentiate highly and poorly metastatic cancers. Histological analysis proved that the porous structure increased the capacity of diagnosis trap to allow more cancer cell infiltration compared to the previous design. The overall results support that diagnosis trap device can be used for diagnosing EC metastasis and, potentially, for reducing LN metastasis.

Chapter 2.
An optical probe for detecting chondrocyte apoptosis in response to mechanical injury

2.1. Abstract

Cartilage injury induced by acute excessive contact stress is common and mostly affects young adults. Although early detection of cartilage injury may prevent serious and lifelong arthritic complications, early detection and treatment are not possible due to the lack of a reliable detection method. Since chondrocyte injury and subsequent cell death are the early signs of cartilage injury, it is likely that cartilage cell apoptosis can be used to predict the extent of the injury. To test this hypothesis, a near-infrared probe was fabricated to have a high affinity to apoptotic cells. *In vitro* tests show that this apoptosis probe has low toxicity, high specificity, and affinity to apoptotic cells. In addition, there is a positive relationship between apoptotic cell numbers and fluorescence intensities. Using mouse xiphoid injury model, we found a significant accumulation of the apoptosis probes at the injured xiphoid cartilage site. There was also a positive correlation between probe accumulation and the number of apoptotic chondrocytes within the injured xiphoid cartilage, which was confirmed by TUNEL assay. The results support that the apoptosis probes may serve as a powerful tool to monitor the extent of mechanical force-induced cartilage injury *in vivo*.

2.2. Introduction

It is estimated that more than 27 million adults in the United States suffer from osteoarthritis, approximately 12% of these individuals have a type of osteoarthritis that develops as a result of a mechanical force-induced cartilage injury (also called as post-traumatic osteoarthritis) [1-2]. Patients with cartilage injury commonly suffer from joint pain and stiffness, reduced mobility and function, poor quality of life, and increased lifetime medical costs [3-6]. Unfortunately, injured cartilage may worsen and remain asymptomatic for years. When symptoms arise, the disease may

have already reached a later, more complicated stage that is compounded by the availability of limited treatment options.

The diagnosis of injured cartilage generally begins with a detailed history, a physical examination, and plain radiographs of the joint. Certain laboratory tests (e.g., synovial fluid tests, computed tomography scans, magnetic resonance imaging) may be useful to confirm the presence of injured cartilage [3, 7]. Magnetic resonance images provide a three-dimensional view of cartilage that may elucidate cartilage irregularities [8]. Because these structural changes can only be appreciated during the intermediate or late stages of cartilage injury, these conventional methods cannot be used to detect early changes within the injured cartilage. It is generally believed that the early diagnosis and prevention of cartilage injury will improve outcomes while reducing disability and associated costs [9]. Therefore, there is an urgent need for a method that will detect cartilage injury at its early stage.

Noninvasive near-infrared (NIR) fluorescent imaging technology has recently been used for the detection of various diseases and physiological conditions, including cancer, arthritis, infection, and cardiovascular disease [10-14]. NIR light can penetrate deeper into tissues (up to 10 cm depending on the tissue types) than visible light because biological tissues absorb less NIR light [15]. In addition, due to less autofluorescence with the use of NIR imaging, a higher signal-to-background acquisition ratio is possible [16]. To exploit the unique features of NIR light for *in vivo* imaging, several optical imaging probes have been developed in an attempt to diagnose cartilage injury during its earliest stages. For example, NIR probes have been prepared to detect cathepsin and matrix metalloproteinases in synovial fluid, because higher levels of these components were found in patients with arthritis [17-19]. Hyaluronic acid–immobilized gold nanoprobes have been used for the *in vivo* monitoring of the high local production of reactive

oxygen species and hyaluronidase in arthritic joints [20]. A folate-targeted NIR probe has been used *in vivo* to image rheumatoid arthritis in mice because the synovial membrane in mice with rheumatoid arthritis has been shown to accumulate large numbers of activated macrophages, which have upregulated folate receptors [21]. In general, these probes have been developed to detect inflammatory responses and products associated with inflammatory arthritis.

On the other hand, chondrocyte apoptosis is well recognized as one of the earliest responses to cartilage injury caused by mechanical trauma and is linked with injury severity [22-25]. Chondrocyte apoptosis has been associated with the production of reactive oxygen species, the shortage of growth factors, the release of glycosaminoglycan, and mechanical injury [22, 26]. As a consequence of chondrocyte apoptosis, loss of resident cells in the articular cartilage occurs and results in the impaired extracellular matrix and potentially, the development of cartilage injury [27-28]. Therefore, we believe that the detection of apoptotic chondrocytes soon after cartilage injury can be used to determine the extent of the cartilage injury that can lead to early treatment and prevention.

Many groups of imaging probes have been developed for the detection of different stages of cell apoptosis. Annexin V [29], synaptotagmin C2A domain [30], and phosphatidylserine-binding peptides [31] have been developed to recognize phosphatidylserine. It was later found that phosphatidylserine may also be present in the outer leaflets of non-apoptotic cells, including activated B and T lymphocytes and mast cells [32]. In addition, a class of apoptosis probes that are classified on the basis of their ability to determine activated caspases have also been described [33-34]. Despite their high specificity, caspase-based probes only recognize intracellular molecules and have to be internalized for detection, which limits their use for *in vivo* imaging. The third group of apoptosis probes is a family of small molecules that includes N, N'-didansyl-L-

cysteine and butyl-2-methylmalonic acid [35-36]. These compounds can selectively bind to transport membranes. They then accumulate in the cytoplasm of apoptotic cells following the permanent loss of their membrane potential, membrane acidification, and phospholipid scrambling [36].

Another class of apoptosis probes is based on a monoclonal antibody that recognizes the La autoantigen, which is present only after the loss of cell membrane integrity during the later stages of apoptosis [37-38]. To improve the ability to detect cell apoptosis *in vivo* during their earliest stages, ApoPep-1—a six-amino-acid peptide (CQRPPR)—has been developed. This probe would target apoptotic cells by binding to histone H1, which is exposed on the surface of apoptotic cells [39-40]. However, it is not clear whether the ApoPep-1 probe can be fabricated for the *in vivo* detection of injured cartilages.

In the current study, an apoptotic cell–detecting probe was synthesized by sequentially coupling NIR dye and CQRPPR into a polyethylene glycol (PEG) polymer. The ability of the probe to bind apoptotic cell was first tested *in vitro* with the use of apoptotic chondrocytes. The effectiveness of the probe to detect chondrocyte apoptosis in injured mouse xiphoid explants was further demonstrated. Finally, this probe was tested for its ability to detect chondrocyte apoptosis *in vivo* using our previously described xiphoid injury mouse model[25].

2.3. Results

The apoptotic cell-detecting probe was prepared, and its structure is schematically shown in Fig. 1A. PEG was introduced into the probe to improve the biocompatibility of the probe and water solubility, as well as to extend its circulation time in the body, as described in previous studies [41-42]. Optical measurement of the probe showed that the probe had a maximum absorbance peak at 755 nm and a maximum emission peak at 787 nm (Fig. 1B). These results showed that the NIR

dye was successfully coupled with the probe. Fourier transform infrared spectra (FT-IR) were created with the use of a Nicolet 6700 spectrometer to determine the chemical structure of the probe. Broadband from 1,620 to 1,660 cm^{-1} for both the peptide and the probe was identified, and the band is typically assigned to the guanidino group of the peptide (Fig. 1C) [43-44]. The FTIR results indicated that the apoptotic cell-binding peptide had been conjugated successfully with the probe.

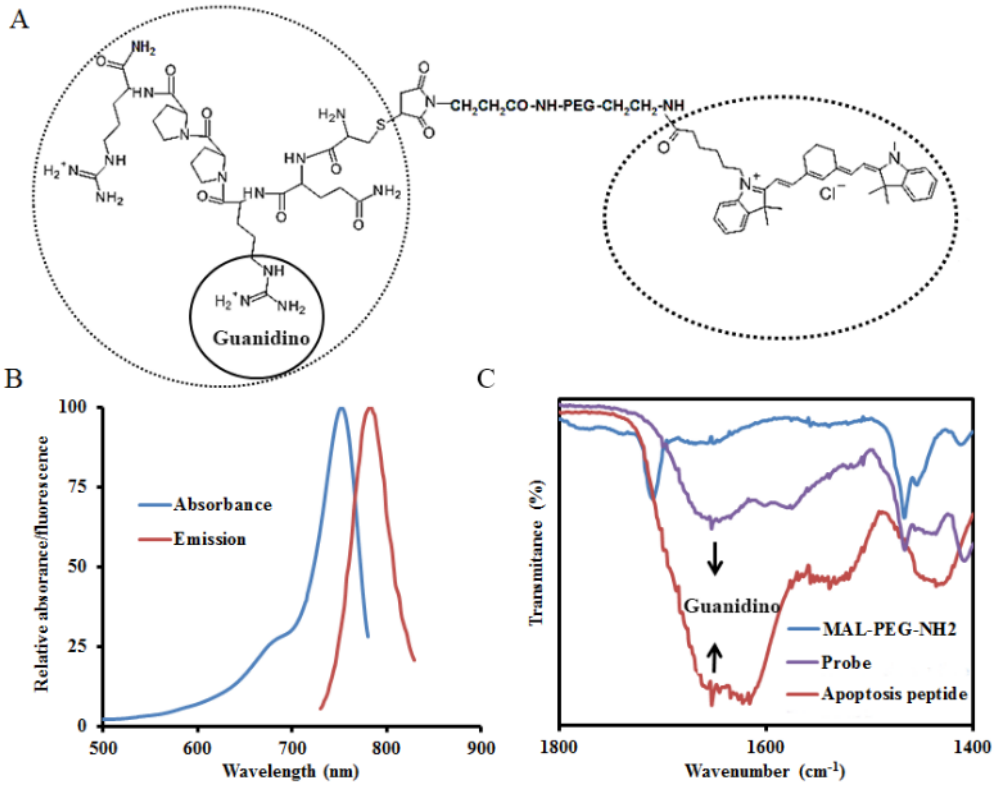

Figure 1. The preparation and characterization of the probe.
(A) Schematic illustration of the probe structure. (B) The optical properties of the probe. (C) Fourier transform infrared spectra of the peptide, the polyethylene polymer, and the probe, respectively.

Next, the cytotoxicity of the probe was tested using bovine chondrocytes and an MTT assay (Fig. 2A). The results of this experiment showed that the probe did not induce statistically significant cytotoxicity to chondrocytes under the concentration of 0.25 mg/mL. On the basis of this result, subsequent studies were carried out using a probe concentration of 0.05 mg/mL. The binding ability of the probe to apoptotic cells was further tested using apoptotic bovine chondrocytes. Bovine chondrocytes were first treated with sodium nitroprusside (SNP) to induce apoptosis. Apoptotic chondrocytes were confirmed using Annexin V Fluorescence 594 (Fig. 2B). Annexin V staining (red color) was found only in SNP-treated cells. Next, to confirm the specificity of the probe, SNP-treated apoptotic chondrocytes were co-stained with Annexin V and the probe. Colocalization of two different markers was observed under a fluorescence microscope (Fig. 2C). Merged picture (yellow) of Annexin V (red) and the probe (green) demonstrated the probe has great specificity to apoptotic cells. Furthermore, the apoptosis-associated fluorescence intensity of the probe was determined *in vitro* (Fig. 2D). One can observe that the fluorescence intensity increases with the increase in SNP-treated chondrocyte number. An increasing number of healthy chondrocytes only contributed a slight increase in fluorescence intensity. There is a very high positive correlation between the number of apoptotic chondrocytes and the fluorescence intensities (Pearson correlation coefficient=0.998 for apoptotic cells and Pearson correlation coefficient=0.962 for healthy cells) (Fig. 2D). Also, there is a significant difference between the fluorescent intensities of apoptotic and those of healthy cells from 20,000 to 500,000 (Student's t-test, $p< 0.05$) (Fig. 2D Insert). This result proves that the probe can still recognize apoptotic cells from healthy cells even if the cell number is as few as 20,000 cells *in vitro*. To further confirm the role of the peptide portion of the probe in the targeting of apoptotic cells, we conducted a competition binding test in which peptides with various concentrations were introduced to the

culture media before the addition of probes (Fig. 2E). As expected, it markedly decreased the fluorescence intensity in the presence of increasing concentrations of peptide. There was an approximate 70% reduction in fluorescence intensity when the peptide (5 mg/mL) was added in the competition tests (ANOVA with Tukey-Kramer's test, $p<0.05$, # and $ indicates $p<0.05$ versus 0 mg/ml and $p<0.05$ versus 0.2 mg/ml, respectively). The results suggested that the probe-to-cell interactions were mediated by the ApoPep-1 peptide rather than by cell phagocytosis. Overall, the *in vitro* studies demonstrated that the probe had a high affinity to apoptotic cells and that it could, therefore, be used to quantify the number of apoptotic cells both *ex vivo* and *in vivo*.

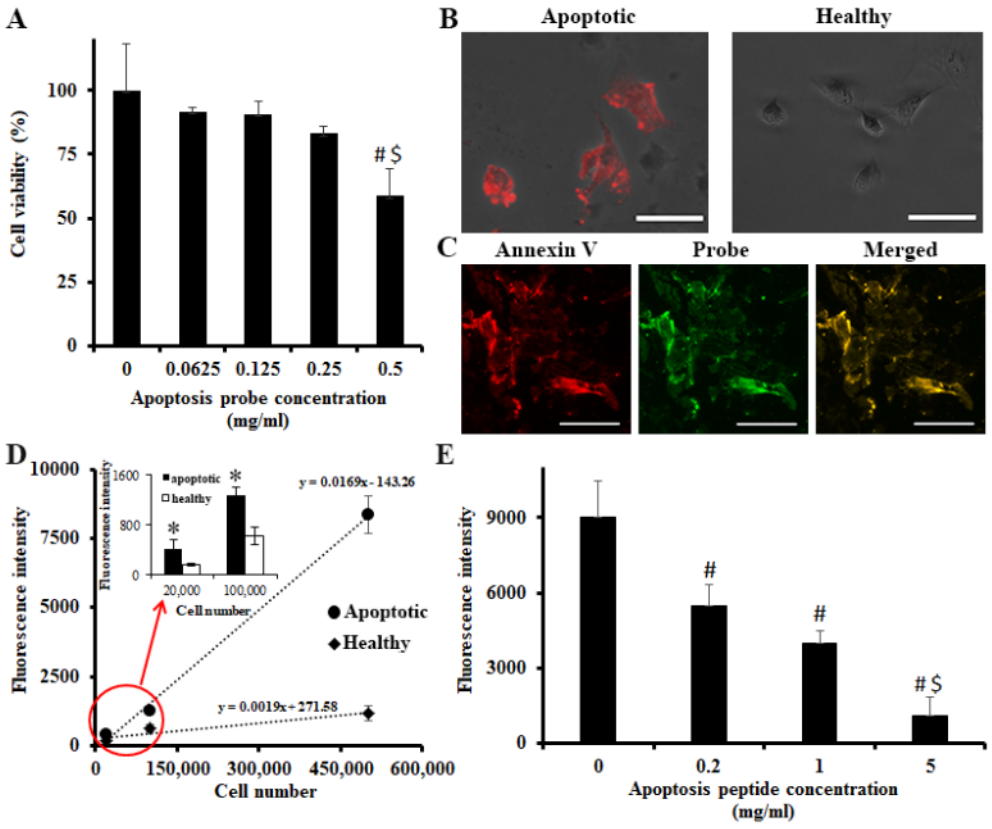

Figure 2. *In vitro* study to assess the cytotoxicity and to evaluate the binding ability.
(A) Cytotoxicity study of the probe to the cells using an MTT assay. (n=5, # and $ indicate $p<0.05$ versus 0 mg/ml and 0.0625 mg/ml, respectively. ANOVA $p<0.05$). (B) Annexin V staining: apoptotic cells (left) and healthy cells (right). Scale bar: 50 μm. (C) Co-staining of SNP-treated apoptotic chondrocyte with Annex V (left), the probe (middle) and their superimposed image (right). Scale bar: 100 μm. (D) The effect of the apoptotic bovine chondrocyte number and healthy

bovine chondrocyte number on the fluorescence intensity. Cell apoptosis induced by SNP (1mM) for 24 hours and probe incubation (0.05 mg/mL) for 30 minutes. (n=5, Apoptotic cells: Pearson coefficient=0.9984 Healthy cell: Pearson coefficient=0.9506). (E) The level of interference of peptides with various concentrations on the binding of the probe to apoptotic cells (500,000 cells per well). Unconjugated peptides were added to block Histone H1 prior to addition of the probe (0.05 mg/mL, 30 minutes incubation) to test probe specificity (n=5, ANOVA $p<0.05$ among groups, # and $ indicate $p<0.05$ versus 0 mg/ml and 0.2 mg/ml, respectively). All the experiments were confirmed statistically using ANOVA with the Tukey-Kramer test or Pearson coefficient. All the statistical data were presented as mean ± standard deviation.

We first assessed whether this probe could be used to detect injured cartilage *ex vivo* with the use of isolated injured xiphoid tissue and controls as drawn schematically (Fig. 3A). We found that after incubating the tissues with the probe at 37°C for 2 hours, there was significantly greater fluorescence intensity from the areas of the xiphoid where the clamp had been applied (Fig. 3B). Quantification analysis showed a four-fold greater fluorescence intensity in the injured xiphoid as compared to the control tissue (Student's t-test, * $p<0.05$) (Fig. 3C). As demonstrated in a previous study, TUNEL staining revealed that mechanical compression indeed triggered chondrocyte apoptosis (Fig. 3D) [23]. Using a fluorescence microscope, we found that probe accumulation on the surface of the injured tissues indeed was much more than control tissues (Fig. 3D). Correlation analysis showed a very high positive relationship between fluorescence intensity and apoptotic chondrocyte number (Pearson correlation coefficient: 0.919) (Fig. 3E). These results support the notion that this probe could be used as an indicator to identify injured cartilage in *vitro* early in the degeneration process.

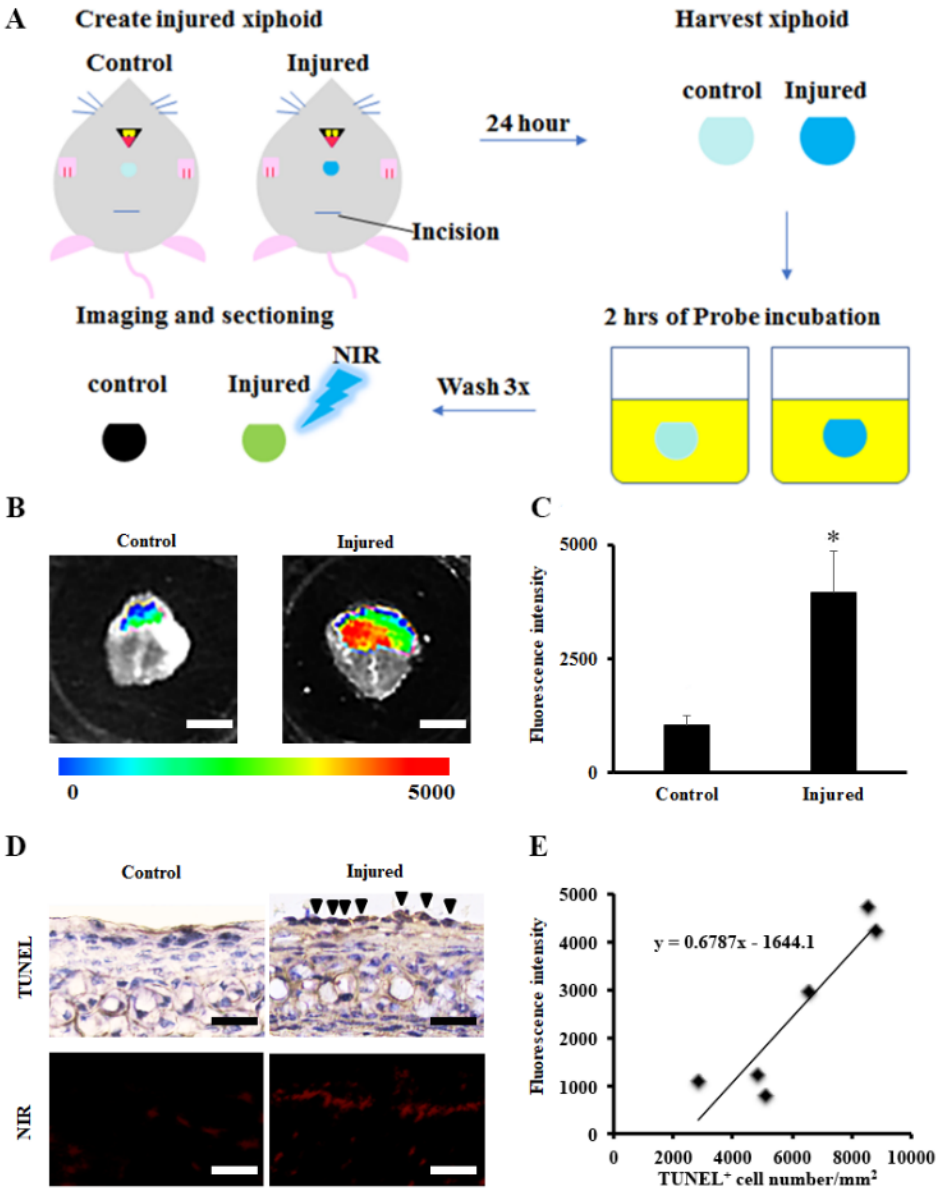

Figure 3. *Ex vivo* study to assess the targeting ability of the probe.
(A) A schematic illustration of the ex vivo injured xiphoid model. (B) Ex vivo imaging of injured xiphoid tissue. Probe incubation (0.05 mg/mL) for 2 hours. Scale bar: 2 mm. (C) Quantification analysis (n=5, Student's t-test, * $p<0.05$). Statistical data was presented as mean± standard deviation. (D) TUNEL staining of injured cartilage explants and control tissue and Near-infrared fluorescence images of injured and healthy (control) xiphoid tissues sections (Scale bar: 100 μm. Arrowheads indicate TUNEL positive cells). (E) Correlation between fluorescence intensity and apoptotic chondrocyte number per 1 mm^2. Pearson correlation test was performed (Pearson coefficient=0.9193).

Next, we used a mouse model to investigate whether the probe was able to detect apoptotic chondrocytes using a mechanically triggered injured xiphoid model *in vivo*. Four days after the xiphoid was injured, the apoptosis probe (100 μL at 0.05 mg/mL) was administered intraperitoneally. *In vivo* images were captured on the fifth day after xiphoid injury (Fig. 4A). We found that the probe accumulated considerably more in injured xiphoid tissues than in control specimens. Fluorescence intensity in the injured xiphoid was approximately five times higher than that of the control group. To further verify that the signal came from the xiphoid, mice were euthanized, and their xiphoids were isolated for additional *ex vivo* imaging. Although the signal intensity for *ex vivo* imaging was a little lower than that of the *in vivo* imaging, the signal-to-noise ratio was profoundly higher (8×, Student's t-test, * $p<0.05$) (Fig. 4B) as compared with that of the *in vivo* imaging (5×, Student's t-test, * $p<0.05$) (Fig. 4A). TUNEL staining was performed to quantify the numbers of apoptotic chondrocytes and cell numbers were normalized to 1 mm^2. Approximately 8 times more TUNEL-positive cells (apoptotic cells) were observed in the injured xiphoid tissue as compared with the control tissue (Fig. 4C). These experiments confirmed that the apoptosis probe could be used to detect injured cartilage undergoing injury-related degeneration in an otherwise intact animal.

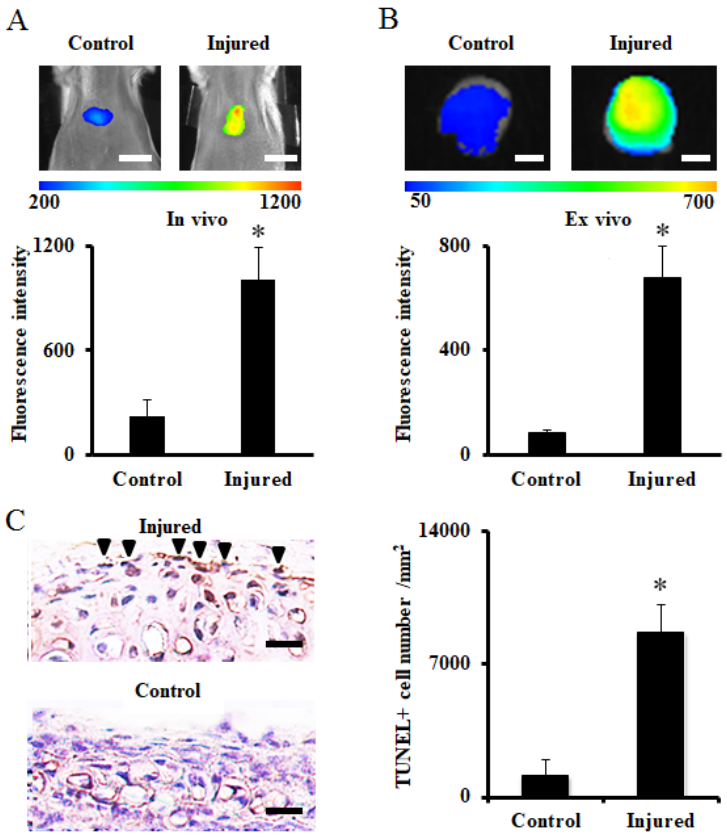

Figure 4. ***In vivo*** **imaging of the xiphoid injury mouse model.**
(A) The merged fluorescence signal with a white-light image captured on the fifth day after xiphoid injury. Probe injection was performed at a concentration of 0.05 mg/mL 24 hours before imaging (top) and the quantification analysis of signal intensity (bottom). Scale bar: 1.0 cm. (B) *Ex vivo* imaging of xiphoid tissue (top) and the quantification analysis (bottom). *Ex vivo* xiphoid samples were isolated from *in vivo* mouse model after imaging. Scale bar: 2.0 mm. (C) TUNEL staining of xiphoid (left) and the quantification analysis (right) (Arrowheads indicate TUNEL positive cells). Where the number of TUNEL positive cells was counted and normalized to 1 mm^2. All the data were calibrated with Student's t-test (n=5, *p<0.05). Scale bar: 100 μm. All the statistical data were presented as mean ± standard deviation.

We examined the potential use of apoptotic probes to monitor recovery after xiphoid injury. The probes were administered 24 hours before the *in vivo* imaging detection was performed. As predicted by our early observations, strong fluorescence appeared only at the injured xiphoid sites

but not at the control sites (Fig. 5A). Interestingly, strong fluorescence signals were able to be observed at the injured xiphoid sites between Day 1 and 7 after injury (Student's t-test, * indicates $p<0.05$ versus control) (Fig. 5A and B). The reduced fluorescence intensity that occurred after Day 14 suggested the reduction of the apoptotic cartilage cells and the recovery of the cartilage tissues; these findings are in agreement with the histological evaluation results (Student's t-test, * $p<0.05$) (Fig.5C).

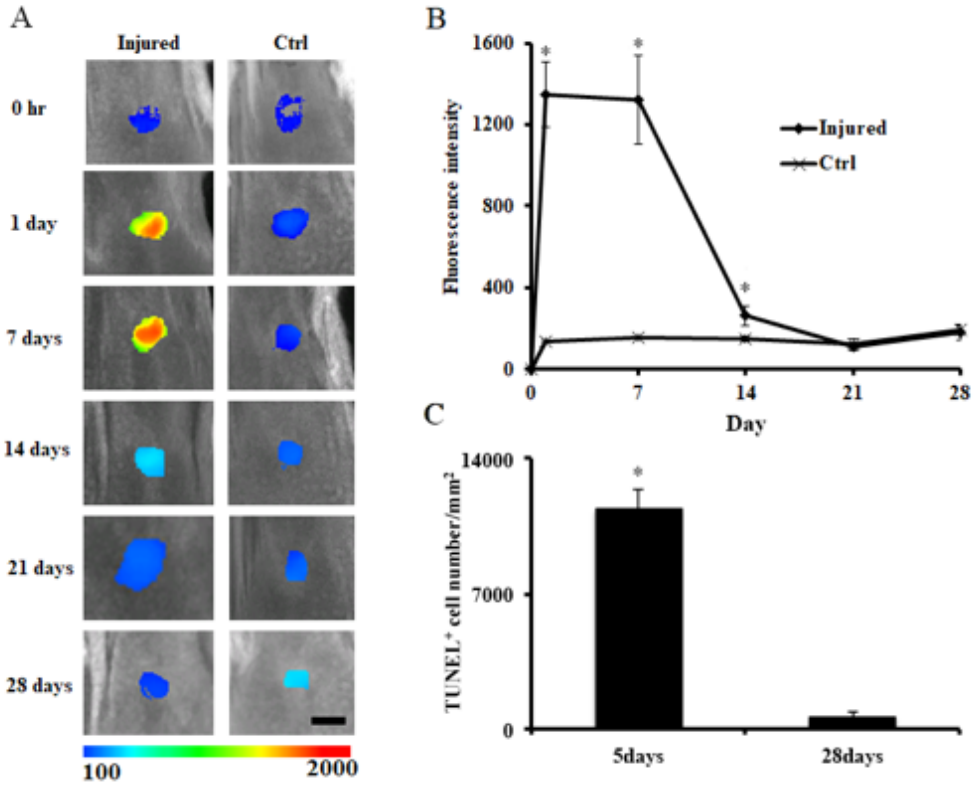

Figure 5. Dynamic monitoring of the xiphoid injury mouse model.
(A) In vivo imaging over time. Sequential images were captured from the same mouse. Scale bar: 4.0 mm. (B) Fluorescence intensity changes at different time points after probe injection (n=5, Student's t-test, * indicates $p<0.05$ versus control). (C) Quantitative analysis of apoptotic xiphoid cells. After the NIR images were taken at the specific time points (Day 5 and Day 28), the animals were sacrificed and xiphoid tissues were isolated for histological analyses and cell number quantification. TUNEL positive cells were counted and then normalized to 1 mm^2. (n=5, Student's t-test, * $p<0.05$). All the statistical data were presented as mean ± standard deviation.

2.4. Discussion

The molecular design of the NIR imaging probe was very critical for in vivo imaging. In this investigation, a histone H1-targeting peptide—CQRPPR—was chosen as a targeting ligand for apoptotic cells. Previous studies demonstrated that the H1-targeting peptide could bind H1 that is exposed on the surface of apoptotic cells [39-40]. Based on the peptide, several probes had been designed for the diagnosis of tumor apoptosis, myocardial cell death, and cell apoptosis associated with ischemia [45-46]. To fabricate apoptosis probes for injured cartilage detection, PEG polymer was included as a carrier to reduce nonspecific binding and to enhance bioavailability and clearance. An NIR dye, Sulfo-Cyanine7, was selected for its deeper penetration depth and its lower rate of an absorbance into the gaps of tissues with improved probe sensitivity [16].

In vitro binding tests of apoptotic cells demonstrated that the probe had strong binding ability to apoptotic chondrocytes. Competition experiments further revealed the critical role of the targeting peptide for the probe to bind apoptotic cells. These results suggest that the binding of the probe to apoptotic cells occurred through their interactions with histone H1 on the surfaces of apoptotic chondrocytes, which was in agreement with the results of previous studies [45-46]. Our xiphoid injury model was used to investigate whether apoptotic chondrocytes could be detected using the probe [25]. *Ex vivo* imaging experiments confirmed that the probe could be used to identify and assess the extent of chondrocyte apoptosis induced by mechanical compression. There is also a positive relationship between the extent of fluorescence intensity and the number of apoptotic chondrocytes. These results suggest that the probe could be used not only to detect chondrocyte apoptosis but also to estimate the extent of the apoptotic chondrocytes.

Finally, via the intraperitoneal administration of the apoptosis probe, *in vivo* imaging was carried out to evaluate the effectiveness of the probe for the detection of chondrocyte apoptosis *in vivo*.

Our results have shown that there was significantly more probe accumulation at the injury sites as compared to control sites. By continuously monitoring the probe's affinity for xiphoid tissue at different time points, we found that apoptotic cells were most prominent between Day 1 and 7 after injury. The probe accumulation at the injured xiphoid sites was drastically reduced after Day 14, which suggests the loss of apoptotic chondrocytes from the xiphoid tissue after clamp-induced mechanical injury.

Our results show great promise regarding the use of the probe for the *in vivo* identification of chondrocyte apoptosis. However, it should be noted that xiphoid injury is not completely identical to articular cartilage injury that would occur in a joint such as the knee. Further experiments will need to be performed using an animal model of articular cartilage injury to investigate whether the probe can detect apoptotic chondrocytes in recently injured articular cartilage. Furthermore, the tissue penetration depth of the NIR signal (could be up to 10 cm depending on the tissue types) [15] may limit the probe's application in clinical practice. Although this shortcoming can be mitigated with the use of NIR arthroscopy [47], the cost and pain generated by the invasive procedure may still negate the probe's usefulness. Therefore, the probe may need to further be modified and optimized for other noninvasive imaging modalities (e.g. positron emission tomography, magnetic resonance imaging) [42, 45, 48] in order to directly visualize the injured cartilage.

In conclusion, an apoptotic cell-detecting optical imaging probe based on a histone H1-binding peptide has been developed to target apoptotic cells. The probe has a high affinity for apoptotic chondrocytes *in vitro* and for the mechanical force–associated cartilage explants *ex vivo*. With the use of a xiphoid injury model in mice, we found that the probe was able to detect apoptotic cells associated with injured xiphoid *in vivo*. These results demonstrate that the probe may provide a

rapid noninvasive imaging technique for the diagnosis of cartilage apoptosis associated with post-traumatic OA.

2.5. Methods

An apoptotic cell-binding peptide (CQRPPR) (United BioSystems Inc., Herndon, VA); a sulfo-cyanine7 N-hydroxysuccinimide ester (Cy7®, Lumiprobe Corp., Hallandale Beach, FL); and a heterobifunctional maleimide polyethylene glycol amine (Mw:3.5k, Mal-PEG-NH2) (JenKem Technology USA, Plano, TX) were purchased. All other chemicals used in this investigation were purchased from Sigma-Aldrich Corporation (St Louis, MO).

2.5.1. Preparation of the apoptotic cell-detecting probe

The apoptotic cell-detecting probe was prepared by the conjugation of CQRPPR and NIR dye onto both ends of the polyethylene glycol amine. Specifically, dye and Mal-PEG-NH2 were dissolved in phosphate-buffered saline (PBS; pH 8.5) at a 2:1 molar ratio and incubated at room temperature overnight. After removing the unconjugated dye by dialysis against deionized water, dye-labeling PEG was collected via freeze-drying. The dye-labeling PEG and peptide were dissolved in PBS (pH 7.2) at a 1:20 molar ratio and incubated overnight at 4°C. After dialysis against deionized water, the probe was lyophilized and stored at 4°C for further use. Absorbance and fluorescence spectra of the probe were measured with the use of an ultraviolet-visible spectrophotometer (Lambda 19 Spectrometer, Perkin Elmer, MA) and an Infinite M200 microplate reader (Tecan, San Jose, CA), respectively. The probe was further analyzed with the use of a Nicolet 6700 FT-IR spectrometer (Thermo Nicolet Corp., Madison, WI). To stain cells for microscope observation, some apoptosis probes were also prepared with Cy5® dye (sulfocyanine7 N-hydroxysuccinimide ester).

2.5.2. Cytotoxicity of the probe

The cytotoxicity of the probe to cells was determined via MTT assay as described previously [49-50]. Bovine chondrocytes were isolated from the patella-femoral grooves of calves using previously established protocols [51]. Briefly, calf knee joints were harvested from a local abattoir less than 36 hours after slaughter. Articular cartilage for *in vitro* study was collected from the patella-femoral grooves of only one donor, minced to approximately 1 mm^3 piece, and digested with 2 mg/mL collagenase type II (Worthington Biochemical Corp., Lakewood, NJ) in Dulbecco's Modified Eagle's Medium with 1% penicillin–streptomycin–fungizone (Life Technologies Corp., Carlsbad, CA) at 37°C overnight. The chondrocyte solution was filtered through a 70 μm cell strainer, centrifuged, and then cultured in Dulbecco's Modified Eagle's Medium (DMEM). Six thousand cells were plated into each well of a 96-well plate and incubated overnight (37°C), and then probes at various concentrations were added to the plate. After 24 hours of probe incubation (0 to 0.5 mg/ml), the MTT assay was carried out with the use of a SpectraMax 340 spectrophotometer (Molecular Devices, Sunnyvale, CA).

2.5.3. Fluorescence microscopy

To stimulate chondrocyte apoptosis, sodium nitroprusside (SNP) was used as described previously [52]. Briefly, bovine chondrocytes were incubated with SNP (1mM) in DMEM for 24 hours. To determine SNP-induced apoptosis, these SNP-treated chondrocytes were stained with Annexin V Fluorescence 594 (Molecular probes, Eugene, OR) following the manufacturer's protocol. Further, the SNP-treated apoptotic chondrocytes were co-stained with Annexin V and the Cy5-labeling probe (0.05 mg/mL, 30 minutes). After washing 2X with PBS, cells were observed on a Leica DMi8 Fluorescence microscope (Leica, Wetzlar, Germany). Cy3 and Cy5 channels were used

detecting Annexin V Fluorescence 594 and Cy5-probe, respectively. All the microscopic images were captured under 200x magnification and analyzed with ImageJ.

2.5.4. *In vitro* assessment of the probe's affinity for apoptotic cells

To assess the ability of the probe to detect apoptotic bovine chondrocytes *in vitro*, the SNP-treated apoptotic chondrocytes and untreated chondrocytes (from 20,000 to 500,000 cells per well) as described above were incubated with the probe (10 μL at 0.05 mg/mL) at 37°C in the 96-well plate. After 30 minutes of probe incubation, each well was washed three times with PBS (pH 7.4) to remove the unbound probes. Apoptosis-associated fluorescence intensities were then determined via the Infinite M200 microplate reader at an excitation wavelength of 760 nm and an emission wavelength of 830 nm. For blocking tests, various concentrations of CQRPPR peptides were added to the chondrocyte-seeded wells (500,000 cells per well) and incubated for 10 minutes before the addition of the probe (10 μL at 0.05 mg/mL). After 30-minute incubation with the probe, the fluorescence intensity was then measured after excessive probes were removed with 3-time PBS washing.

2.5.5. *Ex vivo* and *in vivo* evaluation of the apoptotic probe using the xiphoid injury model

To investigate whether the probe could detect apoptotic chondrocytes in injured cartilage, we employed a previously validated model that made use of mouse xiphoid cartilage explants [25]. All animal experiments were approved by the University of Texas at Arlington Animal Care and Use Committee (IACUC) and in accordance with the Animal Welfare Act and the protocol is consistent with the Guide for the Care and Use of Laboratory Animals. In addition, all research involving animals must comply with the Public Health Service "Policy on Humane Care and Use of Laboratory Animals". The animal procedure is summarized below. Briefly, Balb/c mice (6 to 8 weeks old) were obtained (Taconic Farms, Inc., Germantown, NY) for each study. To trigger

xiphoid chondrocyte apoptosis *in vivo*, the mice were anesthetized, and an incision (1 cm) was created in the midline of the upper abdomen. The exposure was furthered with the use of iris scissors. The xiphoid was then injured by clamping for 2 minutes with a modified Kelly hemostatic clamp (tip, 9.2 mm long × 4.6 mm wide; item no. BH443R; Aesculap, Inc., Center Valley, PA), as previously described[25]. For control purposes, identical incisions were made on additional mice without clamping of the xiphoid. As an *ex vivo* test, several of the animals were euthanized, and the xiphoid tissue was harvested. The injured and uninjured (control) xiphoid tissues were incubated with probes (0.05 mg/mL) for 2 hours. The injured cartilage was washed three times with PBS (pH 7.4), and then *ex vivo* imaging was performed with a Kodak *In Vivo* FX Pro system at an excitation wavelength of 760 nm and an emission wavelength of 830 nm. For *in vivo* evaluation, mice were first divided into injured and control groups. *In vivo* injured xiphoid model was created by clamping the xiphoid structure for 2 minutes. But no damage was made in control groups. On the fourth day after the injury, the probe (100 μL at 0.05 mg/mL) was injected intraperitoneally into two groups of mice. 24 hours later, *in vivo* images were taken and xiphoid cartilages were obtained from mice. To confirm probe accumulation, *ex vivo* images of xiphoid were also captured. For long-term observation, xiphoid injury in mice was created and then images were immediately taken at Day 0. For the next few weeks, the probe (100 μL injection at 0.05 mg/mL) was administered every time before each image was taken at different time frames. Twenty-four hours later after injection of the probe, *in vivo* images were captured using a Kodak *In Vivo* FX Pro system under the same imaging condition.

2.5.6. Immunohistochemistry and histology

To directly assess the xiphoid tissue for evidence of apoptosis, injured and uninjured specimens were embedded in optimal cutting temperature (OCT) compound. The xiphoid sections (8 μm in

thickness) were made in a rostrocaudal manner. TUNEL staining was carried out to determine the presence of apoptotic cells. Apoptotic cells were then labeled in accordance with the manufacturer's instructions (TUNEL Apoptosis Detection Kit; GenScript, Piscataway, NJ). In brief, sections were first fixed in 4% paraformaldehyde/PBS, and then sections were incubated with TUNEL Reaction Mixture following blocking process (3% H_2O_2) and permeabilization step (0.1% Triton X-100 in 0.1% sodium citrate). After reacting with Anti-fluorescein Antibody Solution, sections were incubated in DAB substrate solution. Between all the steps, sections washed with PBS several times. TUNEL Apoptosis Detection Kit contains most of the reagents except fixation buffer, blocking solution and permeabilization solution. Hematoxylin was used for counter-staining. The images were taken under a microscope (Leica). Using ImageJ, TUNEL positive cells were counted per field of view (200x magnification) under the same area (1760 μm^2) from different sample sections as cell density. All quantification data for histological analysis were normalized to cell number per mm^2.

2.5.7. Statistical analysis

ANOVA with Tukey Kramer's test was used to perform the statistical analysis for all the data obtained from the different treatment groups. All the *in vitro*, *ex vivo* and *in vivo* experiment was repeated 5 times. Differences were designated as statistically significant when $P \leq 0.05$ (Student's t-test). Pearson correlation coefficient was also conducted to reflect the relationship between fluorescence intensities and apoptotic cell numbers *in vivo*. All the statistical results were presented following the format of mean ± standard deviation. ANOVA and with Tukey-Kramer test was analyzed in Fig. 2A and Fig. 2E. Pearson coefficients for Fig. 2D and Fig. 3E was calibrated. Student's t-test was performed in Fig. 3C, Fig. 4, Fig. 5B and Fig. 5C.

Chapter 3.

Chemokine releasing particle implants for trapping circulating prostate cancer cells

3.1. Abstract

Prostate cancer (PCa) is the most prevalent cancer in U.S. men and many other countries. Although primary PCa can be controlled with surgery or radiation, treatment options of preventing metastatic PCa are still limited. To develop new treatment of eradicating metastatic PCa, we have created an injectable cancer trap that can actively recruit cancer cells in the bloodstream. The cancer trap is composed of hyaluronic acid microparticles that have good cell and tissue compatibility and can extend the release of chemokines to 4 days *in vitro*. We find that erythropoietin (EPO) and stromal derived factor-1α (SDF1α) can attract PCa *in vitro*. Animal results show that EPO-releasing cancer trap attracted many circulating PCa and significantly reduced cancer spreading to other organs compared with controls. These results support that cancer trap may serve as a unique device to sequester circulating PCa cells and subsequently reduce distant metastasis.

3.2 Introduction

It is estimated that 174,650 new cases will be diagnosed with PCa in 2019 and almost 10% of or 31,620 patients are expected to succumb to this disease [53]. The major cause for the mortality of PCa patients is due to the onset of metastatic PCa to the bone, lymph nodes, liver and lung [54-59]. The common diagnostic tests are the PSA test, transrectal ultrasound, and prostate biopsy test. There are several treatment options available. Androgen deprivation therapy has been shown to be beneficial, albeit in the stage of metastasized PCa [60]. However, cancer cells acquire resistance and become incurable at the late stage [61,62]. Although radiation and targeted therapies can be very effective to control peripheral invasion [63,64], these approaches are not able to control those

metastatic cells that might have spread into circulation [65-67]. In addition, many of the current regimens therapies significantly affect the quality of life of patients by causing various side effects [68-70]. It is, therefore, of utmost importance to develop new strategies that can diminish PCa metastasis with minimal side effects.

We believe that a new strategy should be developed to attract circulating PCa cells and thus reduce PCa spreading. Inspired by the success of roach motels that control cockroach infestations, our design is to attract migrating cancer cells using specific chemokines that can preferentially recruit metastatic cancer cells into "roach motel-like" cancer traps. These traps are composed of degradable, injectable polymeric microparticles capable of releasing bait (cancer-specific chemokines). Injectable microparticles are made of hyaluronic acid (HA), a natural material with great biocompatibility and biodegradability [71,72] Two chemokines/growth factors, SDF-1α and EPO, are included as the "bait" based on the following early observations. SDF-1α and EPO are found to affect cancer cell migration [73-75]. In addition, EPO is found to promote the recruitment of a wide variety of cancer cells, including prostate, melanoma, lung, and breast [74].

This work summarizes our effort on the design and characterization of the PCa cancer trap. HA microparticles were synthesized and used as the base of our cancer trap. We first investigated the physical properties, drug-releasing kinetics, and cytotoxicity of HA particles. To assess the ability of the cancer trap to preferentially attract metastatic PCa cells, we used both PC3 (poorly metastatic) and DAB2IP-knockdown PC3 (highly metastatic, abbreviated as KD) cells [76]. We tested the efficacy of the subcutaneously implanted cancer trap to recruit intravenously inoculated PCa cells

in vivo. Finally, by comparing the PCa cell biodistribution in animals with or without cancer trap implants, we assessed the influence of cancer trap implant on cancer cell metastasis.

3.3. Results

3.3.1. Chemotactic activities of different chemokines and growth factors

To explore the idea of fabricating cancer traps for PCa cells, our first task was to identify the chemokines/growth factors that are potent in promoting PCa recruitment. Based on the literatures, EPO [74], SDF-1α [75], CCL5 [77], VEGF-C [78], CCL2 [79] and CCL16 [80,81], as a control were selected as potential candidates. Using Transwell cell migration system, we first determined the chemotactic ability of EPO (100 U/ml), SDF-1α (100 ng/ml), CCL5 (100 ng/ml), VEGF-C (100 ng/ml), CCL2 (100 ng/ml), and CCL16 (100 ng/ml) using highly metastatic KD cells and poorly metastatic PC3 cells. The concentrations for each chemokine and growth factor with the highest chemotactic activities were chosen based on the manufacturer's information. Our results have shown that, as expected, KD cells are more sensitive to all biomolecules than parental PC3 cells at any given concentrations. On the other hand, SDF-1α and EPO are the most potent cytokines of inducing the migration of KD cells (Fig. 6A). Subsequent studies were carried out to demonstrate the effect of EPO (Fig. 6B) and SDF-1α (Fig. 6C) on the migratory ability of KD compared with PC3 cells in a dose-dependent manner.

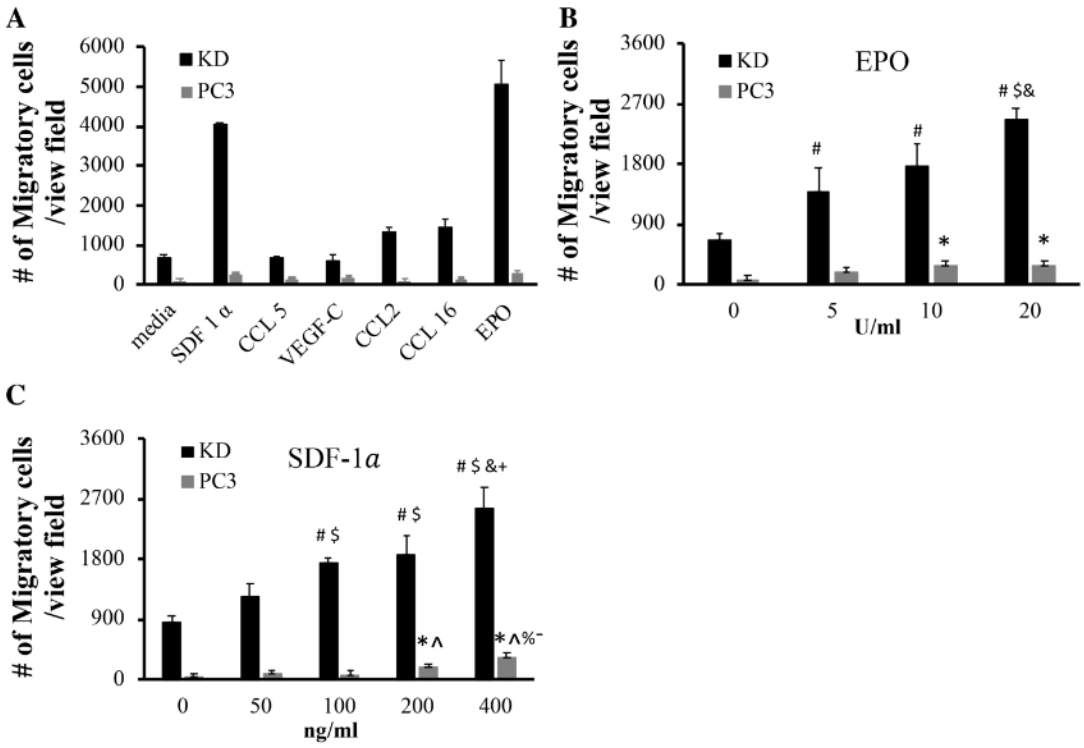

Figure 6. The effects of chemokines on cancer migration.
The in vitro migration of PCa cells under different chemokines and growth factors was determined using the Transwell system. The studies were carried out using either PC3 or KD cells. (A) Migration of KD cells treated with different chemokines and growth factors –EPO (100 U/ml), SDF-1α (100 ng/ml), CCL5 (100 ng/ml), VEGF-C (100 ng/ml), CCL2 (100 ng/ml) and CCL16 (100 ng/ml) was determined. (B) The influence of different concentrations of EPO (ANOVA $p< 0.05$ among groups of KD and PC3 cells. #, $ and & indicate $p< 0.05$ versus 0, 5 and 10 U/ml in KD cells and * indicates $p< 0.05$ versus 0 U/ml in PC3 cells, respectively.) and (C) SDF-1α (ANOVA $p< 0.05$ among groups of KD and PC3 cells. #, $, & and + indicate $p< 0.05$ versus 0, 50, 100 and 200 ng/ml in KD cells and *, ^, % and - indicate $p< 0.05$ versus 0, 50, 100 and 200 ng/ml in PC3 cells, respectively.) on the migration of KD and PC3 cells. Data are mean ± SD (n = 5). Experiments were confirmed statistically using ANOVA with the Tukey-Kramer test.

3.3.2. Characterization of HA particles

HA microparticles were fabricated and used as a chemokine reservoir of cancer trap. To reduce particle migration and cell internalization, the micron-sized scaffolds were fabricated using an

emulsion polymerization technique with DVS (Divinyl Sulfone) used as a crosslinker (DVS: HA= 6.33:1 molar ratio). The microparticles have a spherical appearance under a fluorescence microscope and scanning electron microscope (Fig. 7A, C). The majority of the HA particles have sizes ranging from 1.6-12 μm (Fig. 7B). From the FTIR spectrum of synthesized HA particles, we find that the stretching vibration of sulfone (≈1300 cm^{-1}) appears and bending vibration of alkenes (≈780 cm^{-1}) disappears on the particles after HA polymers are crosslinked by DVS (Fig. 7D).

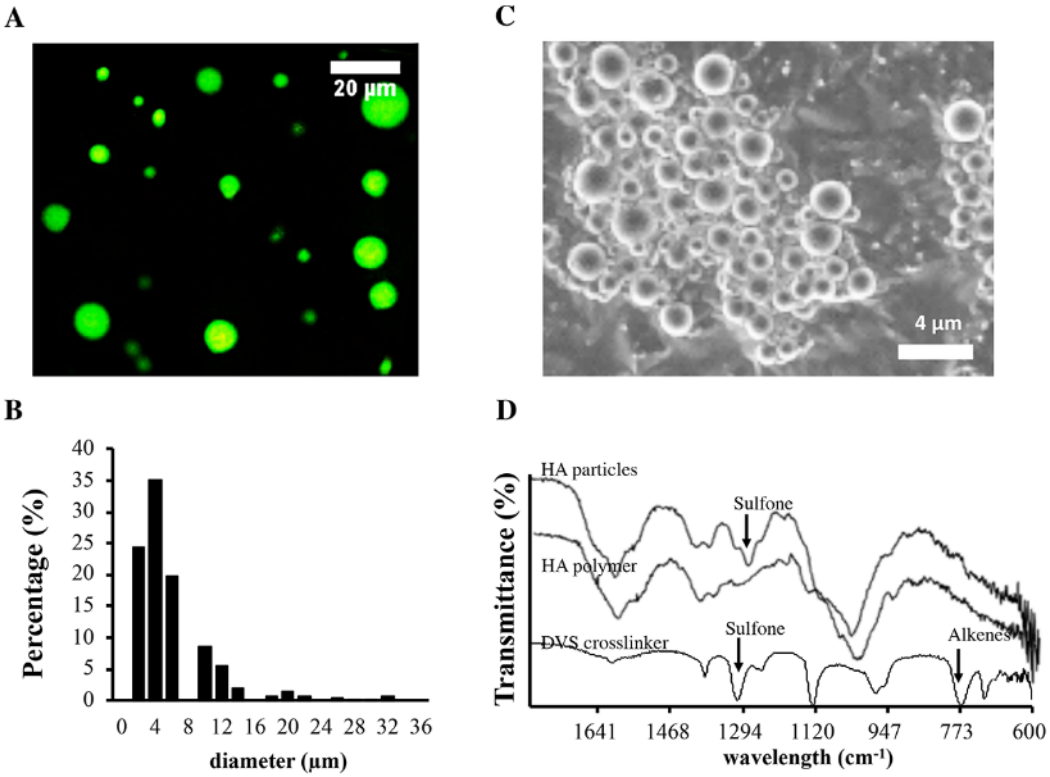

Figure 7. Properties of hyaluronic acid particles.
The physical and chemical properties of hyaluronic acid (HA) particle with high crosslinking density (DVS: HA=6.33:1) were characterized. (A) Morphology and B) size distribution of HA particles were documented under a fluorescence microscope. The sizes of 200 HA particles were compiled to determine the size distribution of HA particles. (C) Scanning electron microscope images of HA particles. (D) IR spectrum of HA particles, HA (700K) polymers, and DVS crosslinker. It illustrates that stretching vibration of sulfone (≈1300 cm^{-1}) appears and bending vibration of alkenes (≈780 cm^{-1}) disappears after HA polymers are crosslinked with DVS.

3.3.3. Slow release property, loading capacity, and cell and tissue compatibility of HA particles

The chemokine loading capacity and releasing capability of HA particles were evaluated *in vitro*. The loading capacities of HA particles were 17.5 μg EPO/ mg particles and 1.23 μg SDF-1α/ mg particles when the initial loading concentration was 20.0 μg EPO/mg and 1.60 μg SDF-1α/mg particles, respectively. In an *in vitro* system, we find that the amount of released EPO and SDF-1α reached to 55% (55 μg) and 63% (5.0 μg) loading capacity of HA particles within 4 hours. After 4 hours, EPO and SDF-1α-loaded HA particles released at a relative slower speed of 0.32% (0.32 μg)/hour and 0.08% (0.0062 μg)/hour, respectively (Fig. 8A).

We found that HA particles have no apparent toxicity of up to 1 mg/mL *in vitro* (Fig. 8B). The tissue compatibility of HA particles was evaluated using a mouse subcutaneous implantation model and PLGA particles were used as controls. After implantation for 2 days, we found that, by comparing with PLGA particles, HA microparticles prompted significantly less inflammatory cells accumulation near implantation site (Fig. 8C) based on H&E staining and less $CD11b^+$ macrophage recruitment (Fig. 8D). Also, there is a low extent of inflammatory cells accumulation was observed at HA microparticles implantation and saline injection site, suggesting that HA particles have good tissue compatibility.

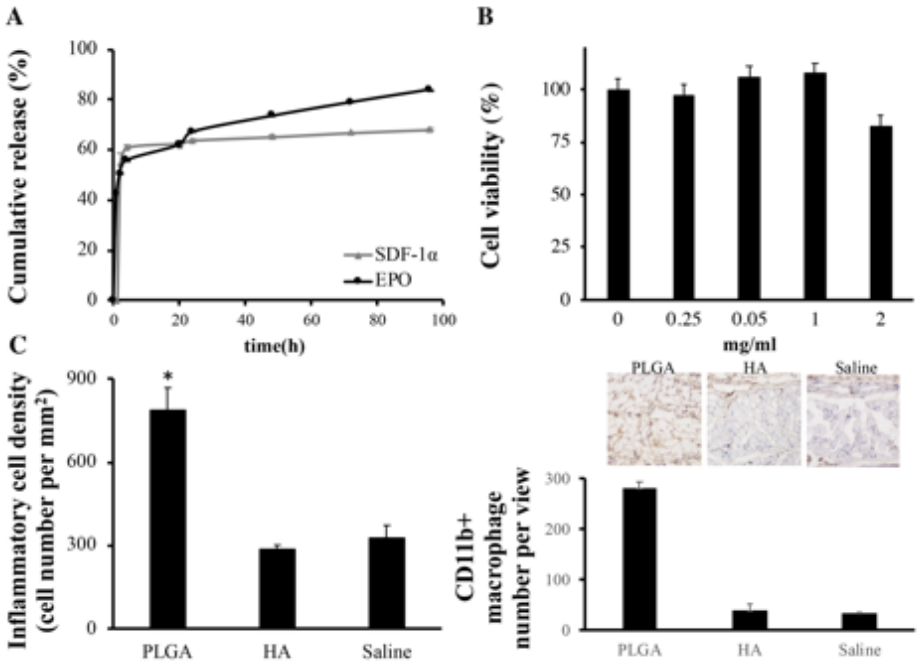

Figure 8. Slow release property and cell/tissue compatibility of HA particles.
The slow release property, cell, and tissue compatibility of hyaluronic acid (HA) particles with crosslinking densities (DVS: HA=6.33:1, labeled as "HA") were characterized. (A) The release rate of Cy5 labeled EPO or SDF-1α (Cy5-EPO or Cy5-SDF-1α) was quantified *in vitro*. (B) The cell compatibility of HA particles was determined using 3T3 fibroblasts *in vitro* (n = 5). (C) The tissue compatibility of HA particles was measured *in vivo* using a subcutaneous implantation mice model. The overall number of inflammatory cells were counted based on H&E staining. (D) The number of $CD11b^+$ macrophages was counted after IHC staining and Hematoxylin counterstaining. The density of inflammatory cells surrounding particle implants was quantified histologically to reflect the extent of tissue compatibility of different particle implants (100x magnification). (n = 3) Data are mean ± SD. (Student's t-test, * indicates $p < 0.05$ versus Saline group.)

3.3.4. *In vivo* assessment of cancer trap

To investigate the capability of cancer trap, EPO-loaded and SDF-1α-loaded HA particles were administered in the subcutaneous cavity. After particle implantation for 12 hours, mice were IV injected with NIR-labeled cancer cells. The distribution of cancer cells was then monitored via NIR imaging daily for up to 5 days.

Based on NIR fluorescent intensities, we found that the chemokine-loaded HA particle implant recruited significantly more highly metastatic KD cells than poorly metastatic PC3 cells (Fig. 9). The maximal recruitment of KD cells to EPO-loaded HA implants was achieved in 24 hours and then last for 3 days. The total intensity of KD cells from the implanted site was 14,200,000 ± 2,000,000 AU/implant site (about 64,000 KD cells/ implant site) at Day 1 and remained at a similar level until Day 3 with about 57,000 KD cells/ implant site. The fluorescent intensities at the implant site decreased after Day 4 (Fig. 9A). On the other hand, the maximal KD cell recruitment of SDF-1α-releasing HA was found at Day 1 - 12,100,000±4,000,000 AU/implant site (~54,000 KD cells/ implant site). The numbers of cancer cells at SDF-1α-releasing HA implant site reduced substantially (~70%) at day 2, increased slightly at Day 3 (~ 31,000 KD cells/ implant site), and then reduced with time (Fig. 9B). The above results suggest that EPO-releasing traps have the capability to capture and retain cancer cells at the trap implant site for up to 3 days.

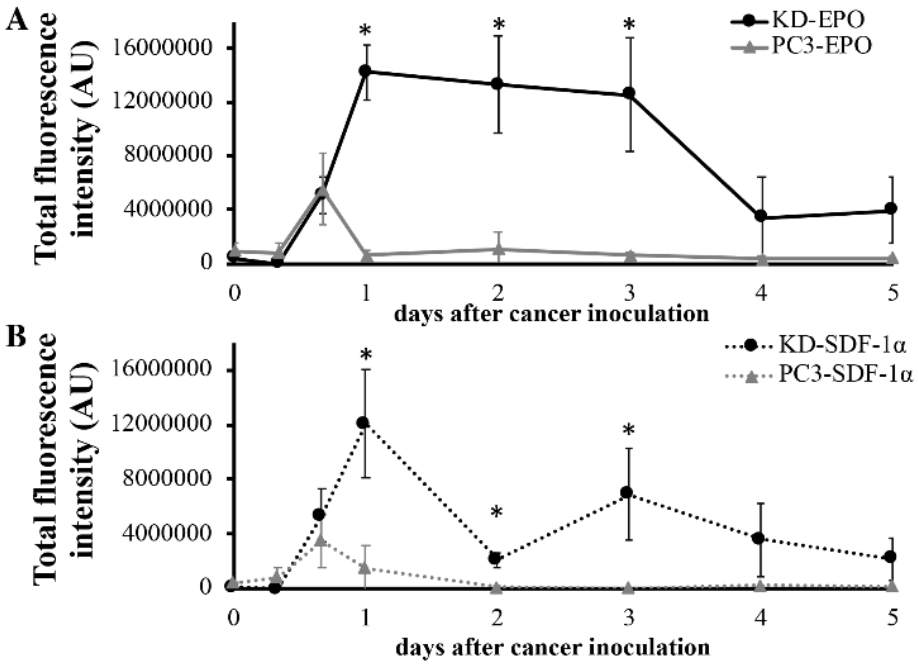

Figure 9. *In vivo* dynamic cancer migration pattern in cancer trap.
The ability of erythropoietin (EPO) and stromal derived factor-1α (SDF-1α)-loaded HA particles to recruit PCa was tested for the different periods of time (8 hours to 5 days) in vivo. We used metastatic KD and parental PC3 cells in this investigation. Quantitative results of cell recruitment to (A) EPO-loaded and (B) SDF-1α-loaded implants at different time points were graphed and compared. (n = 3) Data are mean ± SD. (Student's t-test, *p< 0.05)

To test the hypothesis, we compared the PCa cell recruitment efficiency between the PCa cell recruitment efficiency between SDF-1α- and EPO-loaded implants using the same animal model at Day 2 (36 hours after cancer inoculation). As expected, our results show that EPO implants recruited >7X more KD cells than PC3 cells. In addition, SDF-1α implants attracted ~7X more KD cells than parental PC3 cells (Fig. 10A, B). Nevertheless, EPO implants appear to be slightly more efficient than SDF-1α implants by recruiting ~1.3X more KD cells (Fig. 10A, B).

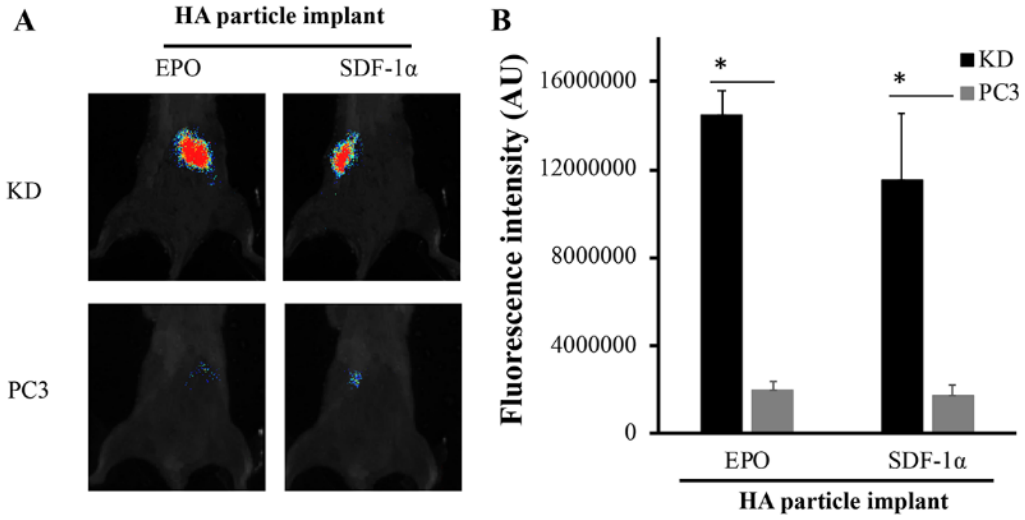

Figure 10. Optimization of cancer trap.
The efficiency of EPO-loaded and SDF-1α-loaded particles to recruit metastatic KD and parental PC3 Qtracker-labeled cancer cells was evaluated *in vivo*. (A) After cancer inoculation for 36 hours, whole animal images were taken. (B) The fluorescent intensity at the particle implant sites was quantified. The estimated number of KD cells at EPO and SDF-1α particle implant sites are 67,000 and 53,000 cells per implant, respectively. The estimated PC3 cells at EPO and SDF-1α particle implant sites are 8,960 and 7,750 cells per implant, respectively. N = 3 in all groups. Data are shown as mean ± SD. (Student's t-test, *p< 0.05)

3.3.5. Evaluation of the localization of PCa cells inside or surrounding of cancer trap

The recruitment of KD cells in cancer trap was examined histologically. GFP^+ KD cells were used in this study. In addition, GFP^+ KD cells were labeled with Vybrant DiD cell labeling dye (with an excitation wavelength: 649 and emission wavelength: 670nm). Tissue sections of EPO-loaded particle implants (EPO + HA) and particles alone (HA) were imaged for its NIR signals. We found significant NIR signals surrounding EPO-loaded particle implant sites (Fig. 11A). Most of the signals are at the interface of particle implants and surrounding host tissue. These results support that ability of EPO-loaded particles enhanced the recruitment of KD cells migration toward the implants. By overlapping NIR and fluorescent images, we determine that NIR signals coincide with GFP suggesting the presence of live KD cells in the around the particle implants (Fig. 11A, B). We found that there are significant more NIR signals in the EPO-loaded particle implants (EPO + HA) than particles alone (HA) (Fig. 11B). Finally, the numbers of KD cells in tissue sections were quantified. In agreement with an earlier observation, we find the EPO-loaded particle implants (EPO + HA) attracted >3X more KD cells than chemokine-free particle implants (HA) and particle-free tissue controls (Control) (Fig. 11C).

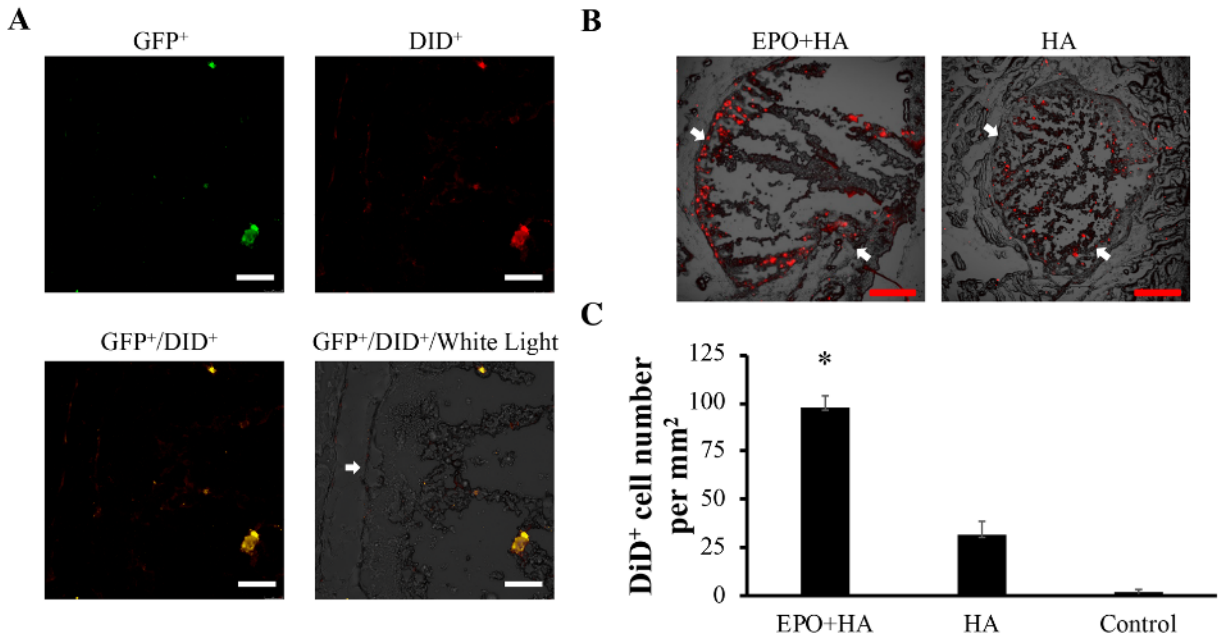

Figure 11. Histological analysis.
Tissue sections were made and imaged to determine the distribution of KD cells in and surrounding particle implants. NIR images of EPO-loaded particles show the presence of DiD-labeled GFP expressing KD cells in and surrounding the implants. HA particles alone and particle-free tissue were used as the negative control. (A) Merged images showed DiD^+ (red) and GFP^+ (green) cells were co-localized in EPO implant (200x magnification). (B) The representative low magnification (25x) of images showed the overlapping fluorescent signals of DiD^+ (red) KD cells in EPO-loaded implant and HA particles alone. (C) Quantification of DiD^+ cells at the site of EPO-loaded particles (labeled as "EPO + HA", 98 ± 6 cells/mm^2), particles alone (labeled as "HA", 31 ± 7 cells/mm^2) and particle-free tissue control (labeled as "Control", 1 ± 2 cells/mm^2). (n = 3) Data are present as mean ± SD. (Student's t-test, *$p < 0.05$ compared to HA.) Scale bar: 100 µm (white) and 300 µm (red). White arrows point to the interface between the skin tissue and the implant and the areas between two arrows are implanted sites.

3.3.6. Impact of cancer trap on cancer cells metastasis

To study the impact of cancer traps on cancer metastasis, EPO-loaded particle implants (EPO + HA) or particle-free tissue control (Control) were implanted subcutaneously (2 implants per animal, 100 µl/site) on the back of mice. After inoculation of KD cells for 36 hours, animals were sacrificed, and all internal organs were imaged using Kodak *in vivo* imaging system (Fig. 12A, B). The

fluorescent intensities of different internal organs were then quantified to reflect the progression of PCa-associated organ metastasis. Noticeably, we found that EPO particles implants significantly reduced KD cell accumulation in the lung (51±4%, $p<0.05$) compared to control (lung: 90±11%) within 36 hours (Fig. 12C). These results suggest that cancer trap device can mitigate the incidence of cancer cell metastasis via circulation. The histological study also uncovers that we found significant fewer KD cells in lung sections with EPO-loaded implants (EPO + HA; estimated 820±430 KD cells/mm^2 view field) than those with untreated control (Control; estimated 44±50 KD cells/mm^2 view field) (Fig. 12D, E). This result supports that cancer traps may lure cancer cells away from circulation and indirectly reduce cancer spreading and/or metastasis.

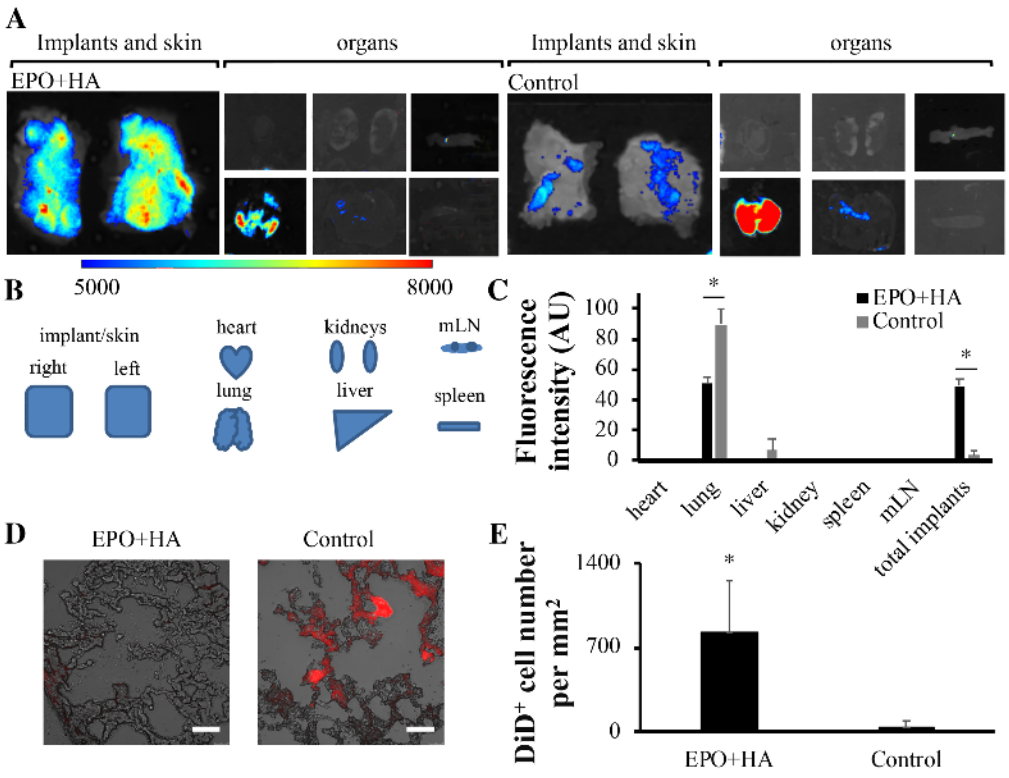

Figure 12. Reduction of cancer metastasis via cancer trap.
Biodistribution of KD cells treated with the EPO-loaded particles or untreated control was quantified based on the measurement of organ-specific fluorescent intensities. To observe the biodistribution, NIR-labeled cancer cells were administered intravenously 12 hours following subcutaneous particles implantation injection or no treatment. (A) NIR imaging of internal organs was imaged 36 hours after cell administration. (B) A depiction of the organ arrangement. (C) The

percentages of the cell distribution in different organs were calculated based on the individual organ fluorescent intensity divided by total internal organ fluorescent intensities. (D) Histological images of the metastatic lung showed the accumulation of KD cells in the lung (400X magnification). Scale bar: 50 μm (E) The lung tissue sections were used to quantify DiD^+ cancer cells in lung sections from animals with EPO-loaded particles (EPO + HA) (829 ± 429.6) vs. untreated control (Control) (44 ± 49.8) groups. (n = 4) Data are mean ± SD. (Student's t-test, *$p<0.05$) Mesenteric lymph nodes are abbreviated to mLN.

3.4. Discussion

Metastasis remains a challenging clinical problem that accounts for the majority of cancer mortality. Tumor progression towards metastasis is governed by a complex multi-step process whereby tumor cells dissociate from their primary site of growth, invade surrounding tissues, intravasate into a blood vessel or lymphatic vessel, survive in circulation, adhere to and extravasate from the vessel and form a new tumor at the secondary site [76,82-84]. Our *in vitro* and *in vivo* studies have demonstrated that EPO and SDF-1α are the most capable of luring metastatic PCa. These results are supported by several recent observations. Specifically, EPO and SDF-1α have been shown to recruit PCa cells [74,85]. It should be noted that our study does not exclude the possibility that other types of cytokines and chemokines may also participate in the migration of PCa. For examples, CCL2 facilitate PCa cell growth and bone metastasis [79].

HA particles were employed to form the cancer trap based on these previous observations. Firstly, since hyaluronic acid dermal filler was approved by the FDA in 2008, studies have shown that biodegradable HA has been proven to have a good safety and cell/tissue compatibility [72,86]. Secondly, HA implants were found to induce minimal inflammatory responses due to their nonimmunogenic properties [87,88]. Thirdly, HA particles can be easily mixed with any

chemokine in aqueous solution with denaturing its bioactivity minimally [89]. Fourth, the degradation rate of HA particles is tunable via crosslinking density. Recent research showed that the maximum duration of HA-based dermal filler reaches up to 12 months and the increase of chemical crosslink density slows down degradation rate for short-term cancer treatment [88,90]. Finally, since HA particles don't respond to the changes of the environment, diffusion, degradation or osmotic pressure are believed to be the main factors to drive the release of drug and protein from HA particles [91].

The present work was focused on the development of cancer traps that can preferentially recruit circulating PCa cells. While our previous work has shown that implant-mediated inflammatory responses can enhance the recruitment of many cancer cells, including PCa [74], our goal is to establish a new technique to attract metastatic PCa cells without eliciting an inflammatory reaction. To achieve the goal, we determine that cancer trap should possess the following three characteristics. First, cancer traps should have good cell/tissue compatibility with minimal foreign body reactions. Second, cancer trap can be injected into the subcutaneous cavity to minimize surgical trauma. Finally, via the slow release of chemokines/growth factor, cancer trap can create localized chemokine gradience to recruit circulating cancer cells.

Our results show that cancer trap not only can recruit metastatic cancer cells but also decrease the accumulation of PCa cells in the lung and liver. These findings support that cancer trap implantation may reduce PCa metastasis and, perhaps, prolong the survival of PCa patients. In fact, it is well established that patients with visceral metastases have a higher mortality rate [92,93]. In addition, metastatic organs of PCa such as lung, liver, pleura, and bone are more commonly found among patients [55]. By repeated administration of cancer traps, it is possible that we can trap numerous circulating PCa in the subcutaneous space and, thus, indirectly delay their spreading

inside the body. In addition, using localized radiation and/or chemotherapy, cancer traps may be developed as a new cancer treatment to eradicate metastatic PCa cells.

3.5. Conclusion

We have developed a new cancer trap using injectable HA-microparticles that can release different chemokines/growth factor to preferentially attract circulating and metastatic PCa cells. Among chemokines tested, EPO and SDF-1α are the most potent cytokines to recruit metastatic PCa cells *in vitro*. From an animal model injected with metastatic PCa cells intravenously, subcutaneously implanted cancer traps are found to able to attract a significant amount of circulating PCa cells and further reduce the presence of circulating PCa cells in several visceral organs, including lung. These results support the potential of cancer traps used in patients with metastatic PCa to reduce or prevent the incidence of distant metastasis.

3.6. Material and Method

3.6.1. Materials

HA (sodium salt, 700KDa) was purchased from Lifecore Biomedical (Chaska, MN, USA). 1-heptanol (1-HP) and Divinyl sulfone (DVS, crosslinker) were obtained from Sigma-Aldrich (St. Louis, MO, USA). Isooctane, dioctyl sulfosuccinate sodium salt (AOT), N-Hydroxysuccinimide (NHS) and 1-Ethyl-3-(3-dimethylaminopropyl) carbodiimide (EDC) were obtained from Fisher Scientific (Waltham, MA, USA). EPO (Epogen® Alpha) was purchased from Amgen Inc. (Thousand Oak, CA, USA). The rest of the chemokines were purchased from Biolegend (San Diego, CA, USA).

3.6.2. Preparation of hyaluronic acid microparticles

HA microparticles were synthesized via a water-in-oil microemulsion process as described earlier with minor revision [94]. Briefly, HA aqueous solution (3 mL, 1.5 wt % in 0.2 M NaOH) was

added dropwise into a 50 mL oil phase solution (isooctane + 0.2 M AOT + 0.04 M 1-HP) and then DVS (15 mM) under homogenization at 28,000 rpm for 5 minutes using OMNI GLH homogenizer (OMNI international, GA, USA). The reaction was allowed to continue under vigorous stirring (2,200 rpm for 1 hour) at the room temperature. The reaction was then stopped with the addition of 3 ml of HCl (0.2 M). The HA microparticles were collected via precipitation in acetone. The crude HA microparticles were then washed consequently with deionized (DI) water, ethanol, and acetone. The purified HA microparticles were completely re-dispersed in DI water and then lyophilized for further use.

3.6.3. Characterization of hyaluronic acid microparticles

To visualize the appearance of the microparticles, some HA microparticles were labeled with CF™488A dye (Biotium, Inc., Fremont, CA, USA) as described earlier [95]. The structure of HA particle is composed of a dense sphere shell and a loose interior to offer a space that contains an aqueous solution [96-98]. The microparticle morphology was observed, and the images were captured using a Leica fluorescence microscope (Leica Microsystems, Germany) equipped with a Nikon E500 Camera (8.4 V, 0.9 A, Nikon Corporation, Japan). The obtained images were used to determine the average size and distribution of particles using Image J [99]. The degree of swelling is also tunable by varying the crosslinking densities [100,101]. Chemokine loading capacity and release kinetics were determined *in vitro* as mentioned in a previous publication [102]. Briefly, Cy5-labeling chemokine (EPO: 100 μg, SDF-1α: 8 μg) was loaded into freeze-dried HA microparticles (5 mg) by a "breathing-in" method [103] when most of the water solution accumulates in the interior space of HA particles and at the same time the size of particles is swelling to bring more solution into HA particles [97,100]. Subsequently, 500 μL of PBS buffer

was added on the top of the HA microparticles incubated at 37°C. At a predetermined time, the supernatant was collected, and the release medium was replaced with an equal amount of the fresh one. The amount of the released chemokine, based on a calibration curve, was measured using a microplate reader (Infinite® M200; Tecan Group Ltd, Switzerland). The cumulative release was calculated as the total amount of released chemokine at a specific time relative to the initial loading amount. The *in vitro* cytotoxicity of the HA microparticles was determined by using MTT assay of 3T3 Swiss albino fibroblast cells (ATCC, Manassas, VA, USA) as described previously [104,105]. The *in vivo* toxicity of the HA microparticles was tested using a mouse subcutaneous implantation model as described earlier [106]. CD11b antibody (Santa Cruz, Dallas, TX, USA) was used to identify all the macrophages near the implants.

3.6.4. Cell culture and migration assay

Early study has shown that DAB2IP gene knockdown in PC3 cell, a poorly metastatic line, increases its metastatic potential (also called as DAB2IP-knockdown PC3 cells or KD cells) [76]. These stable cell lines expressing dual reporter genes (GFP and luciferase) were maintained in RPMI1640 medium (Invitrogen, Carlsbad, CA, USA) containing 5% PBS as previously described [76]. Migration assays were performed in Transwell dishes (Corning Costar, Cambridge, MA, USA) as described earlier [106]. For tracking the cell migration *in vivo*, both PC3 and KD were labeled with Qtracker® labeling kit (Life Technologies, Carlsbad, CA, USA) by following manufacture's instruction as illustrated earlier [107]. For the histological study, Vybrant DiD cell labeling dye (Thermo Fisher Scientific, Waltham, MA, USA) was used to track cancer cells according to the product information for observation under a microscope [108].

3.6.5. *In vivo* cancer cell recruitment

To assess the ability of chemokine-releasing HA microparticles for recruiting PC3 and KD cells, immunocompetent Balb/c mice (Taconic Biosciences, Rensselaer, NY, USA) was used in this study. The animal experiments were approved by the Animal Care and Use Committee (IACUC) at the University of Texas at Arlington in accordance with the Animal Welfare Act and Guide for the Care and Use of Laboratory Animals. Animal procedures also comply with the Public Health Service "Policy on Humane Care and Use of Laboratory Animals". The animal procedure is summarized below. First, HA microparticles were mixed with different kinds of chemokines prior to *in vivo* experiments. Various groups of HA microparticles (9% w/v, 100 µl/implant site) were implanted on the back of animals via a 21-gauge needle. After particle implantation for 12 hours, PCa cells ($5x10^6$ cells/animal) were injected intravenously (IV) into mice. *In vivo* cell migration was monitored using Kodak *In-Vivo* Imaging System FX Pro (Carestream Health Inc., New Haven, CT, USA) as described previously [74,109]. To determine *in vivo* cell distribution, at the end of the study, internal organs were isolated and their associated fluorescence intensities were measured based on the NIR images. Finally, the extent of cancer cell recruitment and “cancer trap” biocompatibility was evaluated histologically as previously described [74].

3.6.6. Statistics

All the data were evaluated using a two-tailed student t-test and presented as mean ± standard deviation. The differences among each group were compared based on ANOVA and Tukey-Kramer test. Differences were designated as statistically significant when $P \leq 0.05$ (Student’s *t*-test).

Chapter 4.

An implantable device for diagnosing esophageal cancer metastasis and disseminated tumor cells

4.1. Abstract

Esophageal cancer (EC) patients often have low 5-year survival rate after the diagnosis of lymph node (LN) metastasis. The inability to diagnose EC earlier is believed to be responsible for the poor prognosis. To overcome such a challenge, this study was aimed at engineering an implantable device capable of intercepting migratory ECs prior to LN metastasis for early EC diagnosis. For that, KYSE-30 cells (high metastatic EC cells with 52% $Her2^+$) and KYSE-70 cells (low metastatic EC cells with 0% $Her2^+$) were used in this investigation. We first discovered that erythropoietin (EPO) is a potent chemotactic agent for EC. Using an *in vitro* cancer invasive assay, we have then determined that EPO induced significantly more migration of KYSE-30 cells than those of KYSE-70 cells. Then a biocompatible and porous cancer capturing device (also called a diagnosis trap) was fabricated to slowly release EPO for capturing EC cancer cells. To test their efficacy, the diagnosis trap was implanted near an axillary LN using an orthotopic cancer implantation model, and the cell distribution responding to the trap implants was monitored using whole-body imaging. As expected, we found a significant migration of EC cells toward the trap implants. In addition, there were more KYSE-30 found at the implant site than KYSE-70. The trap device recovered from the animals can be treated with collagenase type II to recover viable cancer cells. Via flow cytometric analyses, we found that $4.03x10^4$/implant of recovered EC cells possess disseminated tumor cell (DTC) markers $EGFR^+$. The animals with trap implants were found to have lower LN metastasis than the controls based on histological analyses. The overall results support that trap implants can be used for diagnosing EC metastasis and, potentially, for reducing LN metastasis.

4.2. Introduction

The American Cancer Society estimates that in 2019, there will be approximately 17,650 new esophageal cancer (EC) diagnoses and 16,080 deaths due to EC in the US [110]. A major cause of EC mortality is cancer metastasis. Based on the National Cancer Institute's Surveillance, Epidemiology, and End Results database, between 2007 and 2013, the 3 stages of EC (localized/no metastasis, regional/early metastasis, and distant/late metastasis) have 5-year relative survival rates of 43%, 23%, and 5%, respectively [111]. It is believed that the lack of a reliable method for early diagnosis of EC is responsible for its high mortality [112]. Currently, EC is initially diagnosed with endoscopy and biopsy. Upon confirmation of diagnosis, several additional tests may be carried out to determine whether EC has spread to lymph nodes (LNs) and other organs. These tests may include endoscopic ultrasound (EUS), computerized tomography, and positron emission tomography [113,114]. The results of these tests will be used to "stage" EC from 0 to IV. Unfortunately, these imaging modalities cannot detect early stages of EC metastasis. Therefore, there is a dire need in the development of new technology for the early diagnosis of EC metastasis.

The two most common EC are squamous cell carcinoma and adenocarcinoma [115]. LN metastasis is recognized as the earliest sign of EC metastasis and one of the most prognostic factors of EC [112,116,117]. LN metastasis is also well recognized as the single most important prognostic factor in EC and is believed to contribute to poor survival rates [118,119]. For all stages of EC, including early stages, LN metastasis is commonly presented (20%-40%) [117]. Furthermore, patients with a single LN metastasis survive significantly longer than those with two or more LN metastasis [120]. LN metastasis appears to occur along the lymphatic chain [121]. Although imaging modalities such as CT, EUS, magnetic resonance imaging, and fluorine-18

fluorodeoxyglucose PET are used to evaluate LN metastasis [122,123], the sensitivity and specificity of these modalities are still unsatisfactory. Sentinel node biopsy has routinely been used to diagnose LN metastasis of EC. But collecting LN biopsy can only be done during surgeries and sentinel LNs cannot regenerate themselves after removal. In addition, there are many surgical procedure-associated risks such as excess bleeding, infection, and lymphedema. The complexity and vastness of the lymphatic system of the esophagus further contribute to the unreliability of the biopsy results [124]. Due to various locations and depths of esophageal tumors, and the bidirectional flow of the intricate lymph drainage system, the metastasis rate for each LN is hard to predict and define [117]. Furthermore, it has been shown that cancer cell detection for the presence of LN metastasis is more sensitive in a peri-tumoral lymphovascular invasion than blood vascular invasion [125]. It is likely that the sensitivity and specificity of EC metastasis diagnosis would be significantly improved if we could detect lymphovascular invasion of EC.

Recent studies have explored the hypothesis that circulating tumor cells, found in peripheral blood, can be used as a diagnostic or prognostic tool to determine cancer stages and predict the overall probability of survival. Among each CTC, their size, morphology, and surface markers vary after environmental stimulation [126.127]. Many studies have proven that with a combination of other pathological and imaging diagnosis, these CTCs help to prognosis the cancer progression [128-130]. However, the use of CTCs as a diagnostic and prognostic tool has raised some concerns. Specifically, due to their small quantity and the lack of specific biomarkers and specific method for cell isolation, the detection of CTCs is not reliable and may be under-estimated [131-133]. Several recent results showed the pivotal role of disseminated tumor cells (DTCs), a type of circulating tumor cells (CTC), in cancer metastasis in LN and many vital organs [126,134]. In

fact, a study showed that 43% of EC patients (n=136) had DTC detected in their LNs [135]. Unlike circulating cancer cells (CTC), DTCs are correlated to LN metastasis and a high mortality rate [136,137]. DTCs were found to correlate with the survival rate of EC patients [138]. While different types of CTCs in peripheral blood are $EpCAM^+$/pan-$Cytokeratin^+$/$cytokeratin18^+$ [139-141], DTCs in LN can also be stained with $Her2^+$/$CXCR4^+$ [126,138,142,143]. It should also be noted that $EpCAM^+$ DTC, in particular, is highly correlated to lymph node metastasis, cancer stages, and overall survival [124].

While DTCs have been shown to play a critical role in EC LN metastasis, the molecular mechanisms governing DTC responses are mostly undetermined because of the lack of method and devices for isolating large quantity of metastatic DTCs *in vivo*. To overcome this challenge, this work was aimed at developing an implantable device which can capture DTCs for *in vitro* culture and analyses. The design of this device is based on our findings that, by releasing EPO at the subcutaneous space, we could recruit metastatic cancer cells to the implant site [144]. Specifically, a diagnosis trap device, which is composed of a cross-linked porous Gelfoam sponge, was fabricated. The ability of various chemokines and growth factors to trigger EC cell migration was tested and EPO was selected. The ability of the diagnosis trap to release EPO and to recruit EC cells was evaluated *in vitro* and then *in vivo*. After being implanted for different periods of time, the diagnosis trap was recovered for cell isolation using collagenase type II. The presence of EC cells and DTCs in the trap captured cells were characterized and quantified using flow cytometry or IHC.

4.3. Results

4.3.1. Fabrication of the diagnosis trap

To characterize Gelform sponge, we imaged the porous structure of Gelfoam using a Scanning Electron Microscope (SEM, Hitachi). The porosity was determined based on the weight of the ethanol absorbed by the sponge. The porosity of the Gelfoam sponge is around 94%. (Fig.13A) After loading Cy5-EPO, chemokine-loaded Gelfoam was freeze-dried. Chemokine release kinetics was determined for several days. By detecting the released Cy5-EPO, the result shows the porous Gelfoam can release EPO for three days. (Fig. 13B)

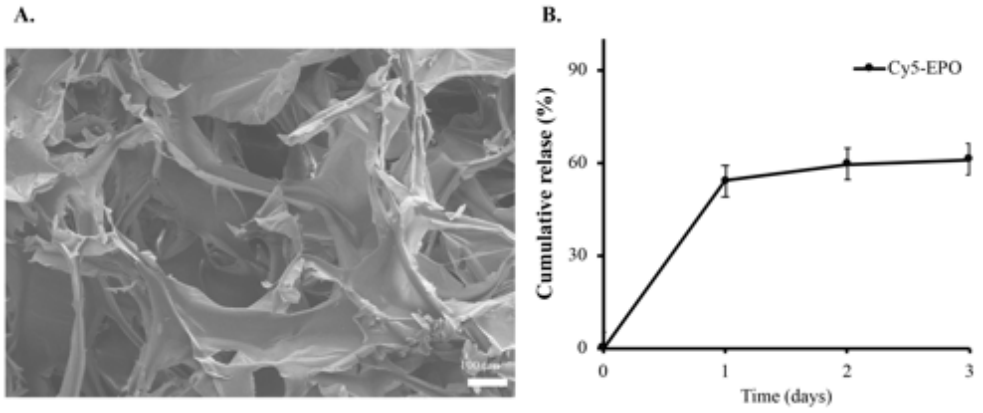

Figure 13. Porous structure and chemokine release property of Gelfoam.
The porous structure and chemokine release property of freeze-dried sponges were characterized. (A) An SEM image of Gelfoam was taken. (B) The release rate of Cy5 labeled EPO (Cy5-EPO) was quantified *in vitro*.

4.3.2. Characterization of EC cells

To fabricate the diagnosis trap, we needed to identify the suitable chemokines or growth factors for facilitating the migration of high metastatic ECs (such as KYSE-30), but not low metastatic ECs (such as KYSE-150). Based on the published results, our initial investigation assessed the

following chemokines, including EPO (200 U/ml), SDF-1α (100 ng/ml), SDF-1β (100 ng/ml), CCL5 (10 ng/ml), CCL2 (10 ng/ml), and CCL21 (50 ng/ml). As expected, all test chemokines and growth factors can promote the migration of KYSE-30 cells (Fig. 14A). Interestingly, our results also revealed that all chemokines, except EPO, induced significantly less KYSE-150 cell migration than KYSE-30 cells (Fig. 14A). Since EPO has the highest potency in promoting EC migration, EPO was selected as the key chemokine for the fabrication of the diagnosis trap.

We analyzed the extent of cell responses on all EC cell types using *in vitro* invasion assay. After 4 hours of incubation, KYSE-30 cells were found to possess a faster invasion rate than KYSE-70, KYSE-270, and KYSE-150. (Fig. 14B) Since $Her2^+$ is a DTC biomarker and $Her2^+$ cancer cells are commonly found in LNs [138,143], we first determined the ratio of $Her2^+$ cancer cells. The microscopic images showed that cultured KYSE-30 cells have a higher ratio of $Her2^+$ cancer cells (52±4%) than cultured KYSE-150 cells (4±2%), KYSE-70 (0%), and KYSE-270 (0%). (Fig. 14C) Since KYSE-30 contains the highest percentage of DTCs, it is likely that KYSE-30 cells possess the highest metastatic potential.

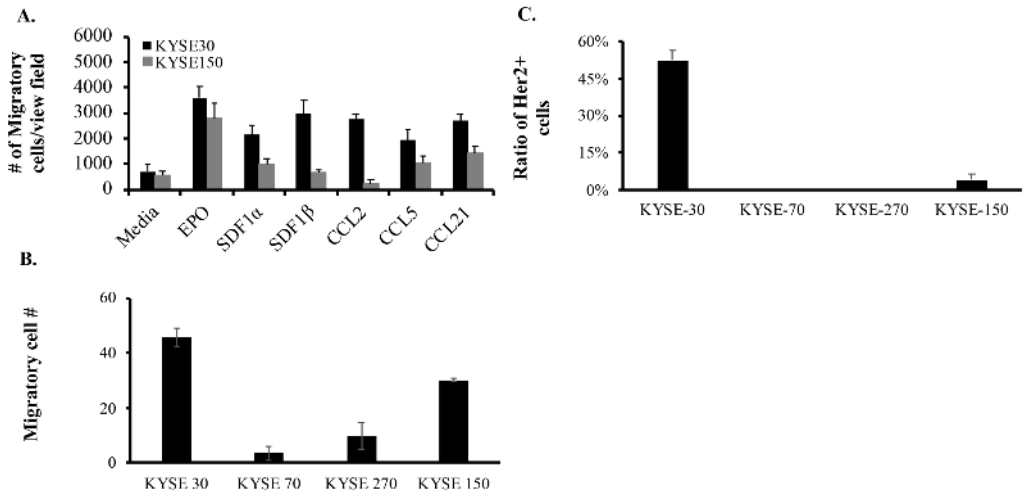

Figure 14. Characterization of 4 different EC cell lines.
(A) The chemotaxis activity of KYSE-30 and KYSE-150 were evaluated using transwell assay to different chemokines: EPO, SDF1α, SDF1β, CCL2, CCL5, and CCL21. More KYSE-30 cells migrate to KYSE-150 under the stimulation of each chemokine. EPO lures more KYSE-30 than KYSE-150. (B) Invasion assays were performed with KYSE-30, KYSE-70, KYSE-270, and KYSE-150 under the stimulation of EPO. (C) Her2 expression on the cell membrane was compared between four different cell lines. Most KYSE-30 cells have higher Her2 expression.

4.3.3. EC recruitment to diagnosis trap in vivo

We evaluated the ability of the diagnosis trap to attract transplanted ECs using the orthotopic implantation model. After EC implantation for 5 days, diagnosis traps were implanted in some animals in the subcutaneous space near axillary LNs. Sham surgery was carried out in some animals as controls. The migration of ECs toward trap implants was monitored using a whole-body imager. NIR images show that there were more KYSE-30 cells ($0.9x10^7$ AU, estimated 29,440 cells) that had migrated to the trap implant than the sham surgical control at Day 1. There was more intensity increase on day 2 ($7.2x10^7$ AU, estimated 222,746 cells). (Fig. 15A) There was no difference between trap implant site and control on the recruitment of KYSE-70 cells on day 1 and 2 (Fig. 15B). By comparing both cell types, we found that the diagnosis trap implants attracted

significantly more KYSE-30 cells than KYSE-70 cells. In addition, diagnosis trap implants are responsible for EC recruitment, since there were significantly fewer cells at the sham surgical site.

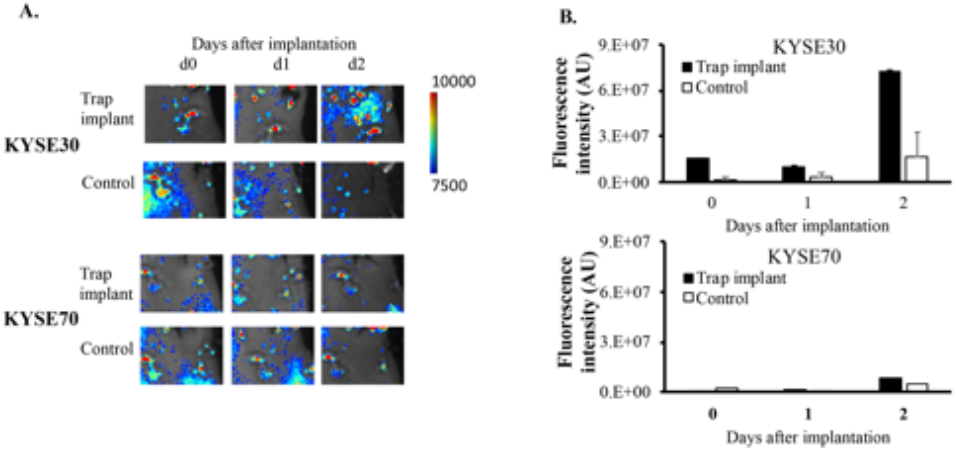

Figure 15. *In vivo* tracking of EC migration-KYSE-30, KYSE-70, KYSE-150, and KYSE-270. After implantation, the migration process of DiD-labeled KYSE-30 and KYSE-70 were monitored. (A) The representative images show the accumulation of ECs around the trap implants. (B) Quantitative results show the stronger recruitment of KYSE30 by the trap implants than those by the control at both day 1 and 2. No differential recruitment was found on KYSE-70.

4.3.4. Influence of trap implants on EC LN metastasis

Since the lymphatic system is an important route for cancer migration, we also examined lymph node metastasis. At the end of the study (with five-day cancer inoculation and two-day cancer entrapment), we isolated various LNs for imaging analyses. Mesenteric LNs in the sham surgical control group have more DiD-labeled cancer cells ($6.6x10^6$ AU) than that in the diagnosis trap group ($2.0x10^6$ AU). (Fig. 16A, B)

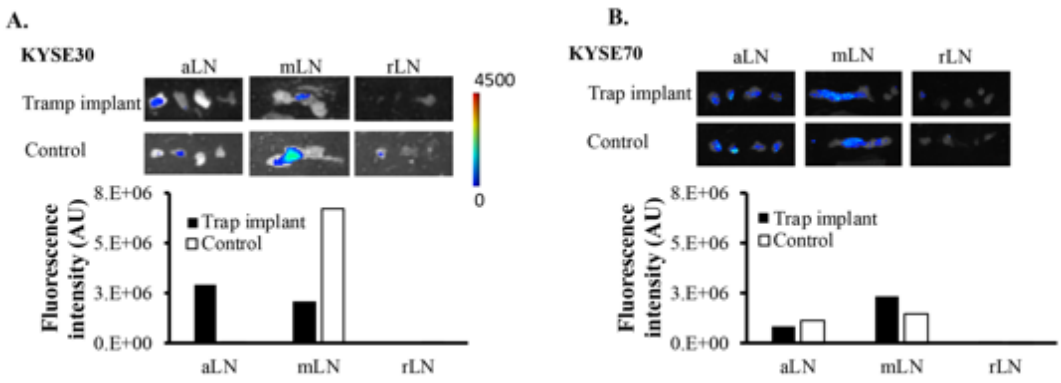

Figure 16. Influence of diagnosis trap implantation on EC LN metastasis.
At the end of the study (with 5 days EC implantation + 2 days trap implantation), animals were sacrificed and various LNs, including axillary LN (aLN), mesenteric LN (mLN), and renal lymph nodes (rLN), were isolated for analyses. (A) Metastatic LNs were observed using a Kodak *in vivo* imaging system. Our cancer trap decreased KYSE-30 cancer migrating to mesenteric LN. Less KYSE-70 cancer cells (Trap implant and control) migrated to LNs. (B) There is more KYSE-30 cell accumulation in sham surgical control groups but less in KYSE-70.

4.3.5. Histological analyses of trap implants

To confirm cancer entrapment, trap implants and LNs were harvested and then histological analysis was performed. As expected, we have found that there are more GFP^+ KYSE-30 inside of the diagnosis trap (809±118 /mm^2) than that of the control (283±54 /mm^2) (Fig. 17A, B). Since Her2 expression status is correlated to the pathologic diagnoses of EC patients [145-147], Her2 is a common marker of DTC in ECs [148,149], and a high percentage of KYSE-30 cells (~50%) are $Her2^+$, subsequent analyses were carried out to survey the distribution of $Her2^+$ EC DTC cells at the implant sites and LN tissues. The LN histological analyses revealed that there were fewer DTCs in the trap implant site (58±16/view field) than in the control group (143±26) [Fig. 5C]. There were also less $Her2^+$ DTC EC cells in mesenteric LN from animals with trap implants than in those animals with sham surgery (Fig. 17C), and the numbers of circulating tumor cells (CTC)

in the blood sample were also quantified after implantation. Interestingly and as expected, trap implantation was found to significantly decrease the number of CTC in serum (91 cells /50 µl blood) by compared to control (267 cells/50µl blood). (Fig. 17D) Overall, the results support our hypothesis that the diagnosis trap implant can recruit ECs and DTCs. Such active recruitment can cause the reduction of EC and DTC presence in LN and blood.

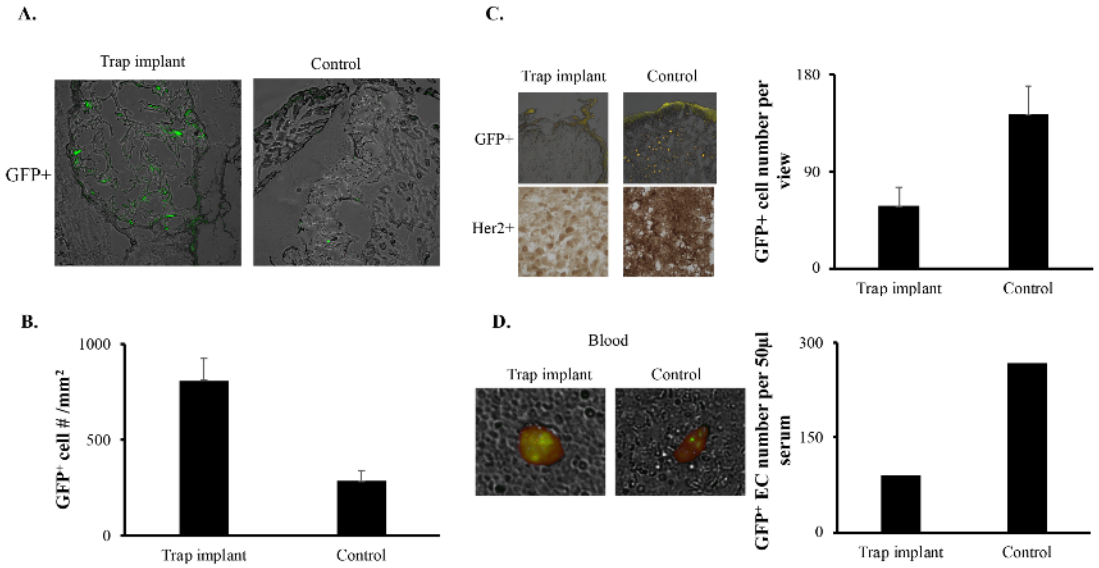

Figure 17. Histological images of the implantation site, metastatic lymph nodes, and serum. (A, B) Representative images of Histological images of cancer trap showed that more GFP^+ KYSE-30 cells were entrapped in cancer than suture control only. (C) The sections of mesenteric lymph nodes were observed using ImageJ and stained with Her2 antibody. Cancer trap decreases the number of GFP^+ DTC and reduces Her2 expression in lymph nodes. (D) The number of GFP^+ CTC were counted under a fluorescence microscope. Cancer trap also decreases GFP^+ CTC in the circulation system.

4.3.6. Characterization of cells recovered from the trap

After implantation for 2 days, the diagnosis trap was recovered and the trap-associated cells were retrieved following collagenase II treatment. We then characterized the retrieved cells using flow cytometry analyses. We first found that the diagnosis trap could recover a large number of

$4.03x10^4$ GFP^+ EC cells. After performing immunocytochemistry, about $2.3x10^4$ $EGFR^+$ DTC EC cells were captured per diagnosis trap within 2 days (Fig. 18A, C). Among retrieved cells, there was a higher ratio of DTC cells (59%), which was higher than those before cancer inoculation (52%) using ICC staining. (Fig. 18A, B and Fig. 13C) These results support that the diagnosis trap can capture EC cells and DTC cells in animals.

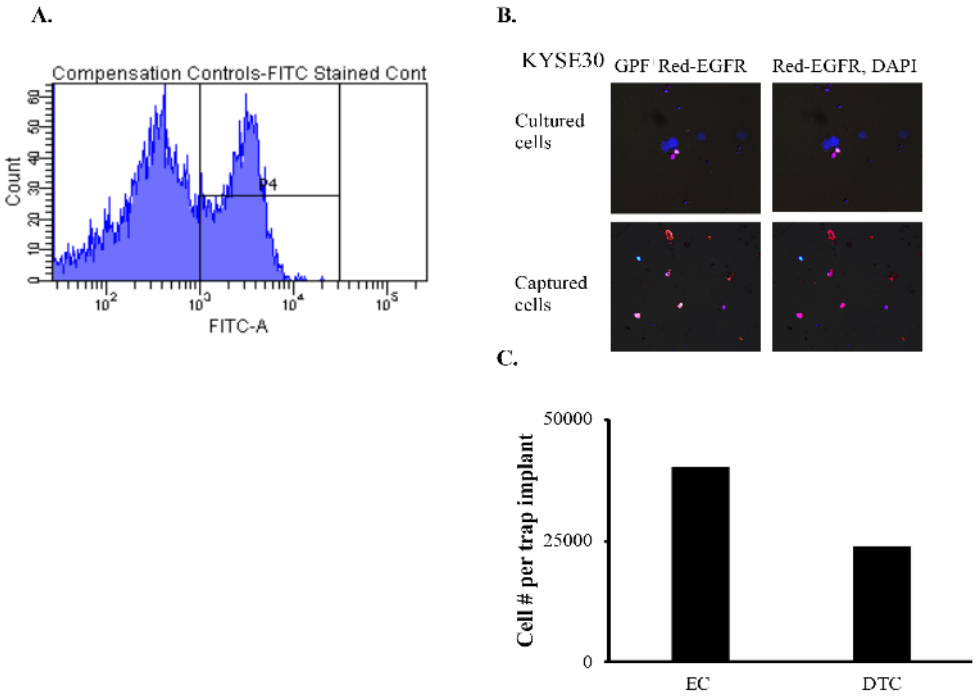

Figure 18. Flow cytometry of captured EC cells

(A) Flow cytometry has proven that 27% of captured cells were GFP^+ KYSE-30. (B) After staining with EGFR protein (DTC biomarker), the fluorescence images showed that GFP^+ captured EC cells express higher EGFR protein than cultured ones. (C) The total number of captured KYSE-30 (EC) and $EGFR^+$ cells (DTC) is around $4.03x10^4$ and $2.3\ x10^4$, respectively.

4.4. Discussion

Here we present a novel device, the diagnosis trap–which can capture implanted EC cells. While we have developed many methods to track the accumulation of cancer cells and tissue *in*

vivo, there are limited methods that have been established for isolating cancer cells from animals or humans. For example, endothelial cell adhesion molecule (EpCAM) antibody (Cellsearch assay) or cell size (ISET) are commonly used in capturing blood CTC. A comparison study for both assays, Cellsearch detects less than 20 cells while ISET can capture less than 70 cells per 7.5ml serum among most prostate cancer patients [150]. The detected cancer cell number is less because of the heterogeneity of serum cancer cells [151]. While we have used these methods in some studies, they have many drawbacks. Specifically, these procedures can only retrieve a tiny number of cancer cells. Because of the lack of sufficient cell numbers, the cells recovered from these methods cannot be used for both research and treatment development. Our results have shown that the diagnosis trap could recover 4.03 $X10^4$ EC cells per implant (equivalent to cells isolated from 4.3 liters blood) and many of these retrieved cells possess DTC cell markers. These findings highlight the significance of this invention for future cancer research and personalized medicine.

The current diagnosis trap design is composed of a porous scaffold and a chemokine. The porous structure allows cell infiltration to improve cell retention. Some suggest that the porous structure provides space for immigrated cancer cells without increasing their malignancy or stimulating cancer proliferation [152,153]. However, further, improvement is needed to facilitate fast cell isolation for culture. By using the property of cancer metastasis, Collagen-based Gelfoam was used as the base of the trap, because the flexible tissue-like structure of Gelfoam has been shown to improve the cell affinity [154]. Since the cancer cell heterogeneity obstructs procedures using antibodies or cell properties to purify serum cancer cells, EPO acts as a chemoattractant to recruit most cancer cells, instead of certain types of cancer, selecting by surface protein expression or cell size. In fact, it has been shown that EC biopsies got from cancer patients have EPO receptor

expression [155]. The porous structure of the cancer trap can provide a spacious room for cell recruitment and retention. This combination helps to recruit large numbers of migrating cancer cells which could be isolated for cancer diagnosis and, perhaps, drug screening.

We found the diagnosis trap to not only attract implanted EC cells but also decrease EC cell migration toward mesenteric LNs. In addition, the histological analysis confirmed that the implantation of the diagnosis trap decreased the number of $Her2^+$ DTC in LNs. Since the accumulation of $Her2^+$ DTC EC cells in LNs are commonly found in patients with late-stage ESCC [156], our results support that we may use the diagnosis trap intercept EC cells from further dissemination and LN metastasis. The most important thing doctors care about is how to diagnose the early stage of cancer. A useful diagnostic tool should be able to determine the early and late stages among patients. So far, our diagnosis trap can capture enough cells for further analysis. But very little we know about the difference between captured cells and the relationship between these cells and cancer malignancy. Our next steps should examine the properties of captured cells to find their correlation to cancer metastasis and then improve the sensitivity of the cancer trap.

4.5. Material and Methods

4.5.1. Cell culture and migration assay

KYSE-30 (obtained from stage III patient), KYSE-150 (obtained from stage II patient), KYSE-70 (obtained from stage II patient) and KYSE-270 (obtained from stage II patient) were human

esophageal cancer cells obtained from the patient' tumor [157,158]. The stable cell lines expressing GFP reporter genes were maintained in 50% RPMI1640 a 50% F-12 medium (Invitrogen, Carlsbad, CA, USA) containing 5% PBS after modifying the previous protocol [157]. A series of chemokines, including EPO (200 U/ml), SDF-1α (100 ng/ml), SDF-1β (100 ng/ml), CCL5 (10 ng/ml), CCL2 (10 ng/ml), and CCL21 (50 ng/ml), were tested on their capability to trigger the migration of EC cells. We performed migration and migration assays in Transwell dishes (Corning Costar, Cambridge, MA, USA) as described earlier [159]. Cell invasion assay was carried out using Collagen type I (BD Biosciences, San Jose, MA, USA) and Transwell dishes (Corning Costar, Cambridge, MA, USA) as described earlier [160]. For tracking the cell migration *in vivo*, EC cells were labeled with Vybrant DiD cell labeling dye (Thermo Fisher Scientific, Waltham, MA, USA) according to the product information, to track cancer cells [161].

4.5.2. Diagnosis of trap fabrication and characterization

Trap implants were composed of porous scaffolds and chemokines. Crosslinking Gelfoam Sterile Sponge (Pharmacia & Upjohn Company, Kalamazoo, MI, USA) were produced based on early work [162]. The biocompatibility of the scaffolds was determined using 3T3 cells as described earlier [163]. The trap implants, chemokine/growth factor loaded scaffolds, were produced by adding EPO (100U/25ul saline) to scaffolds (0.4 cm x0.4 cm x0.5 cm). After being freeze-dried, the EPO-loaded trap implants were ready for study. We recorded the morphology of scaffolds using a Scanning Electron Microscope (Hitachi S-4800 II FE SEM, Hitachi, Japan). We calculated the porosity according to a previous study. [164]

The porosity was calculated using the following equation:

$$\text{Porosity } (\%) = (W_2 - W_3 - W_s)/ (W_1 - W_3) \times 100\%$$

W_1: The weight of absolute ethanol. W_2: The weight of absolute ethanol with immersed sponges. W_3: The weight of absolute ethanol after removing immersed sponges. W_s: The weight of dry sponges.

The releasing rate of chemokine from scaffolds was determined *in vitro* as described in a previous publication [165]. Briefly, Cy5-labelling chemokine (EPO: 100 μg) was loaded into scaffold block (0.4 cm x0.4 cm x0.5 cm). Subsequently, 1000 μL of PBS buffer was added on the top of scaffold block incubated at 37°C. At a predetermined time, the supernatant was collected, and it replaced the release medium with an equal amount of the fresh one. The amount of the released chemokine, based on a calibration curve, was measured using a microplate reader (Infinite® M200; Tecan Group Ltd, Switzerland). We calculated the cumulative release as the total amount of released chemokine at a specific time relative to the initial loading amount.

4.5.3. *In vivo* evaluation of cancer cell recruitment

To assess the ability of the diagnosis trap for recruiting EC cells, we used an orthotopic cancer implantation model as described previously. [166] Immunocompetent Balb/c mice (Taconic Biosciences, Rensselaer, NY, USA) were used in this study since immunocompromised animals have less well established LNs and we want to assess the effectiveness of the diagnosis trap for reducing EC LN metastasis. The animal experiments were approved by the Animal Care and Use Committee (IACUC) at the University of Texas at Arlington under the Animal Welfare Act and Guide for the Care and Use of Laboratory Animals. Animal procedures also comply with the Public Health Service "Policy on Humane Care and Use of Laboratory Animals". The animal procedure is summarized below. First, an orthotopic cancer model was established in which EC cells ($0.5x10^6$) were injected into the esophageal using a 22G needle according to the previous study. Second,

after 5 days of cancer inoculation, diagnosis traps loaded with different chemokines were implanted subcutaneously on the shoulder of animals near axillary LNs. *In vivo* cell migration was monitored using the Kodak *In-Vivo* Imaging System FX Pro (Carestream Health Inc., New Haven, CT, USA) as described previously [144]. After 2 days implantation, the extent of cancer cell recruitment in the diagnosis trap and LNs were evaluated histologically as previously described [144]. To determine *in vivo* cell distribution, at the end of the study, internal LNs were isolated and their associated fluorescence intensities were measured based on the NIR images to estimate the numbers of recruited ECs. To characterize captured cancer cells, 8-µm tissue sections were imaged using a fluorescent microscope. GFP^+ KYSE-30 were counted using ImageJ.

4.5.4. Characterization of cells isolated from the diagnosis trap

At the end of the study (2 days), diagnosis traps were harvested using collagenase type II (Worthington Biomedical Corporation, Lakewood, NJ, USA) at 37 °C for 16 hours and recruited cells in the traps were recovered and then stained with goat anti-EGFR antibody (Santa Cruz Biotechnology, Dallas, TX, USA) and Texas red rabbit anti-goat secondary antibody (Jackson ImmunoResearch, West Grove, PA, USA) before cell cytometry analyses (LSRII Multi-Color Flow cytometry, BD Bioscience, San Jose, CA, USA). The percentages of captured CTCs (GFP^+ KYSE-30) were quantified using flow cytometry and the percentage of DTCs ($EGFR^+$ biomarker) were determined using immunocytochemical staining.

4.5.5. Statistics

All the data was evaluated using a two-tailed student t-test and presented as a mean ± standard deviation. We compared the differences among each group based on ANOVA and the Tukey-Kramer test. We designated differences as statistically significant when $P \leq .05$ (Student's *t*-test).

Chapter 5

Summary and Future work

All these works started from a very interesting observation and no one understood the mechanism at the beginning but tried everything to figure it out. Now we know something and find more things that we still need to spend more time to figure out.

Our first cancer study in Dr. Tang's laboratory started from the inflammation-induced cancer migration. Injectable PLGA particles gave us an idea to design a cancer trap using the chemotactic activity of cancer cells. EPO was one of the chemokines to recruit more cancer cells. However, the inflammatory response caused by PLGA hinders the efficacy of EPO. Inspired by this design, we tested another biocompatible and injectable HA particles to prove our hypothesis. HA particles not only decrease the inflammatory response and their slow release property recruited more cells. The activity of EPO can maintain for several days to differentiate highly and poorly metastatic prostate cancer cells.

Even though more cells were recruited, we are not satisfied with this result. To make the cancer trap more sensitive on detecting migrating cancer cells, instead of using particles, we chose porous Gelfoams as our 3rd generation of cancer trap. The limitation of HA particles is that the particles can only offer the space among particles for cell migration. Most of PCa was accumulated near to the boundary of the tissue and implantation site but not the middle of HA implants. The best pore size for culturing various mesenchymal stem cells ranges from 150-500 μm. [167] It has proven that pore size higher than 300 μm provides a better environment for cell adhesion and cell migration. [168] To increase the capacity, 3D porous structure of Gelform (pore size: 200-500 μm) allows body fluid to penetrate and then bring more cancer cells to disseminate. Two studies have proved that Stage III EC has a higher incidence of lymph node metastasis than Stage II through

pathological analysis. [121, 169] Surprisingly, the *in vivo* study showed that cancer trap can differentiate two different EC cell lines (KYSE-30: Stage III and KYSE-70: Stage II). [157,158]

So far, we can recover captured cancer cells. But the information that these cells represent is still unknown. To learn more about the relationship between captured cancer cells and cancer malignancy, we need to do more tests on these cells to get some clues.

References

1. Lawrence, R. C. *et al*. Estimates of the prevalence of arthritis and other rheumatic conditions in the United States. Part II. *Arthritis Rheum.* **58**, 26-35 (2008).
2. Brown, T. D., Johnston, R. C., Saltzman, C. L., Marsh, J. L. & Buckwalter, J. A. Posttraumatic osteoarthritis: a first estimate of incidence, prevalence, and burden of disease. *J. Orthop. Trauma* **20**, 739-744 (2006).
3. Nuki, G. Osteoarthritis: a problem of joint failure. *Z. Rheumatol*. **58**, 142-7 (1999).
4. Felson, D. T. *et al*. Osteoarthritis: new insights. Part 1: the disease and its risk factors. *Ann. Intern. Med*. **133**, 635-46 (2000).
5. Losina, E. *et al*. Lifetime risk, and age at diagnosis of symptomatic knee osteoarthritis in the US. *Arthrit. Care Res.* **65**, 703-711 (2013).
6. Felson, D. T. The epidemiology of knee osteoarthritis: results from the Framingham osteoarthritis study. *Semin. Arthritis Rheu.* **20**, 42-50 (1990).
7. Mathiessen, A. *et al*. Imaging of osteoarthritis (OA): what is new? *Best Pract. Res. Clin. Rheumatol.* **30**, 653-669 (2016).
8. Borthakur, A. *et al*. Sodium and $T_{1\rho}$ MRI for molecular and diagnostic imaging of articular cartilage. *NMR Biomed.* **19**, 781-821 (2006).
9. Chu, C. R., Williams, A. A., Coyle, C. H. & Bowers, M. E. Early diagnosis to enable early treatment of pre-osteoarthritis. *Arthritis Res. Ther.* **14**, 212 (2012).
10. Ntziachristos, V., Bremer, C. & Weissleder, R. Fluorescence imaging with near-infrared light: new technological advances that enable in vivo molecular imaging. *Eur. Radiol.* **13**, 195-208 (2003).
11. Tang, E. N., Nair, A., Baker, D. W., Hu, W. & Zhou, J. In vivo imaging of infection using a bacteria-targeting optical nanoprobe. *J. Biomed. Nanotechnol*. **10**, 856-863 (2014).
12. Lim, N. H. *et al*. In vivo imaging of matrix metalloproteinase 12 and matrix metalloproteinase 13 activities in the mouse model of collagen-induced arthritis. *Arthritis & Rheumatology* **66**, 589-598 (2014).
13. Chen, J. *et al*. In vivo imaging of proteolytic activity in atherosclerosis. *Circulation* **105**, 2766-2771 (2002).
14. Weissleder, R., Tung, C.-H., Mahmood, U. & Bogdanov, A. In vivo imaging of tumors with protease-activated near-infrared fluorescent probes. *Nature Biotechnol.* **17**, 375-378 (1999).
15. Weissleder, R. A. clearer vision for in vivo imaging. *Nature biotechnol.* **19**, 316-316 (2001).
16. Frangioni J. V. In vivo near-infrared fluorescence imaging. *Curr. Opin. Chem. Biol.* **7**,626-34 (2003).
17. Vermeij, E. A. *et al*. In vivo molecular imaging of cathepsin and matrix metalloproteinase activity discriminates between arthritic and osteoarthritic processes in mice. *Mol. Imaging* **13**, 1-10 (2014).
18. Ryu, J. H. *et al*. Measurement of MMP activity in synovial fluid in cases of osteoarthritis and acute inflammatory conditions of the knee joints using a fluorogenic peptide probe-immobilized diagnostic Kit. *Theranostics* **2**, 198-206 (2012).
19. Lee, S. *et al*. Dark quenched matrix metalloproteinase fluorogenic probe for imaging osteoarthritis development in vivo. *Bioconjugate Chem.* **19**, 1743-1747 (2008).
20. Lee, H., Lee, K., Kim, I. K. & Park, T. G. Synthesis, characterization, and in vivo diagnostic applications of hyaluronic acid immobilized gold nanoprobes. *Biomaterials* **29**, 4709-4718 (2008).
21. Chen, W. T., Mahmood, U., Weissleder, R. & Tung, C. H. Arthritis imaging using a near infrared fluorescence folate-targeted probe. *Arthritis Res. Ther.* **7**, R310-R317 (2005).

22. Hwang, H. S. & Kim, H. A. Chondrocyte apoptosis in the pathogenesis of osteoarthritis. *Int. J. Mol. Sci*. **16**, 26035-26054 (2015).
23. Loening, A. M. *et al*. Injurious mechanical compression of bovine articular cartilage induces chondrocyte apoptosis. *Arch. Biochem. Biophys.* **381**, 205-212 (2000).
24. Huser, C., Peacock, M. & Davies, M. Inhibition of caspase-9 reduces chondrocyte apoptosis and proteoglycan loss following mechanical trauma. *Osteoarthr. Cartilage* **14**, 1002-1010 (2006).
25. Davis, C. G. *et al*. Posttraumatic chondrocyte apoptosis in the murine xiphoid. *Cartilage* **4**, 345-53 (2013).
26. Zamli, Z., Adams, M. A., Tarlton, J. F. & Sharif, M. Increased chondrocyte apoptosis is associated with progression of osteoarthritis in spontaneous guinea pig models of the disease. *Int. J. Mol. Sci.* **14**, 17729-17743 (2013).
27. Thomas, C. M., Fuller, C. J., Whittles, C. E. & Sharif, M. Chondrocyte death by apoptosis is associated with cartilage matrix degradation. *Osteoarthr. Cartilage* **15**, 27-34 (2007).
28. Hashimoto, S., Ochs, R. L., Komiya, S. & Lotz, M. Linkage of chondrocyte apoptosis and cartilage degradation in human osteoarthritis. *Arthritis Rheum*. **41**, 1632-1638 (1998).
29. Blankenberg, F. G. In vivo detection of apoptosis. *J. Nucl*. Med. **49**, 81s-95s (2008).
30. Jung, H. I., Kettunen, M. I., Davletov, B. & Brindle, K. M. Detection of apoptosis using the C2A domain of synaptotagmin I. *Bioconjugate Chem.* **15**, 983-987 (2004).
31. Shao, R., Xiong, C., Wen, X., Gelovani, J. G. & Li, C. Targeting phosphatidylserine on apoptotic cells with phages and peptides selected from a bacteriophage display library. *Mol. Imaging* **6**, 417-426 (2007).
32. Smrz, D., Draberova, L. & Draber, P. Non-apoptotic phosphatidylserine externalization induced by engagement of glycosylphosphatidylinositol-anchored proteins. *J. Biol. Chem.* **282**, 10487-10497 (2007).
33. Zhang, H.-Z. *et al*. N-Ac-DEVD-N‘-(polyfluorobenzoyl)−R110: novel cell-permeable fluorogenic caspase substrates for the detection of caspase activity and apoptosis. *Bioconjugate Chem.* **14**, 458-463 (2003).
34. Liu, J. *et al*. Fluorescent molecular probes V: a sensitive caspase-3 substrate for fluorometric assays. *Bioorg. Med. Chem. Lett.* **9**, 3231-3236 (1999).
35. Aloya, R. *et al*. Molecular imaging of cell death in vivo by a novel small molecule probe. *Apoptosis* **11**, 2089-2101 (2006).
36. Grimberg, H. *et al*. Monitoring of tumor response to chemotherapy in vivo by a novel small molecule detector of apoptosis. *Apoptosis* **14**, 257-267 (2009).
37. Al-Ejeh, F. *et al*. APOMAB, a La-specific monoclonal antibody, detects the apoptotic tumor response to life-prolonging and DNA-damaging chemotherapy. *Plos One* **4**, e4558 (2009).
38. Ayukawa, K. *et al*. La autoantigen is cleaved in the COOH terminus and loses the nuclear localization signal during apoptosis. *J. Biol. Chem.* **275**, 34465-34470 (2000).
39. Wang, K. *et al*. In vivo imaging of tumor apoptosis using histone H1-targeting peptide. *J. Control. Release* **148**, 283-291 (2010).
40. Jung, H. K., Wang, K., Jung, M. K., Kim, I. S. & Lee, B. H. In vivo near-infrared fluorescence imaging of apoptosis using histone H1-targeting peptide probe after anti-cancer treatment with cisplatin and cetuximab for early decision on tumor response. *Plos One* **9**, e100341 (2014).
41. Jokerst, J. V., Lobovkina, T., Zare, R. N. & Gambhir, S. S. Nanoparticle PEGylation for imaging and therapy. *Nanomedicine* **6**, 715-728 (2011).
42. Zhou, J. *et al*. In vivo evaluation of medical device-associated inflammation using a macrophage-specific positron emission tomography (PET) imaging probe. *Bioorg. Med. Chem. Lett.* **23**, 2044-2047 (2013).

43. Liu, W. G., Zhang, J. R., Cao, Z. Q., Xu, F. Y. & Yao, K. D. A chitosan-arginine conjugate as a novel anticoagulation biomaterial. *J. Mater. Sci. Mater. Med.* **15**, 1199-1203 (2004).
44. Jermakowicz-Bartkowiak, D., Kolarz, B. N. & Serwin, A. Sorption of precious metals from acid solutions by functionalised vinylbenzyl chloride-acrylonitryle-divinylbenzene copolymers bearing amino and guanidine ligands. *React. Funct. Polym.* **65**, 135-142 (2005).
45. Kwak, W. *et al*. Apoptosis imaging studies in various animal models using radio-iodinated peptide. *Apoptosis* **20**, 110-21 (2015).
46. Acharya, B. *et al*. In vivo imaging of myocardial cell death using a peptide probe and assessment of long-term heart function. *J. Control. Release* **172**, 367-73 (2013).
47. Spahn, G. *et al*. Near-infrared (NIR) spectroscopy. a new method for arthroscopic evaluation of low grade degenerated cartilage lesions. results of a pilot study. *BMC Musculoskelet. Disord*. **8**, 47 (2007).
48. Guermazi A. *et al*. Synovitis in knee osteoarthritis assessed by contrast-enhanced magnetic resonance imaging (MRI) is associated with radiographic tibiofemoral osteoarthritis and MRI detected widespread cartilage damage: the MOST study. *J. Rheumatol*. **41**, 501-8 (2014).
49. Zhou, J., Tsai, Y. T., Weng, H., Baker, D. W. & Tang, L. Real time monitoring of biomaterial-mediated inflammatory responses via macrophage-targeting NIR nanoprobes. *Biomaterials* **32**, 9383-90 (2011).
50. Tsai, Y. T. *et al*. Optical imaging of fibrin deposition to elucidate participation of mast cells in foreign body responses. *Biomaterials* **35**, 2089-96 (2014).
51. Meretoja, V. V., Dahlin, R. L., Kasper, F. K. & Mikos, A. G. Enhanced chondrogenesis in co-cultures with articular chondrocytes and mesenchymal stem cells. *Biomaterials* **33**, 6362-9 (2012).
52. Chen, Q. *et al*. SNP-induced apoptosis may be mediated with caspase inhibitor by JNK signaling pathways in rabbit articular chondrocytes. *J. Toxicol. Sci.* **37**, 157-67 (2012).
53. Siegel, R. L., Miller, K. D. & Jemal, A. Cancer statistics, 2019. *CA Cancer J. Clin.* **69**, 7-34, doi:10.3322/caac.21551 (2019).
54. Tannock, I. F. *et al.* Docetaxel plus prednisone or mitoxantrone plus prednisone for advanced prostate cancer. *The New England journal of medicine* **351**, 1502-1512, doi:10.1056/NEJMoa040720 (2004).
55. Shen, M. M. & Abate-Shen, C. Molecular genetics of prostate cancer: new prospects for old challenges. *Genes Dev.* **24**, 1967-2000, doi:10.1101/gad.1965810 (2010).
56. Wang, S. *et al.* Prostate-specific deletion of the murine Pten tumor suppressor gene leads to metastatic prostate cancer. *Cancer Cell* **4**, 209-221, doi:10.1016/S1535-6108(03)00215-0 (2003).
57. Koo, K. C. *et al.* Predictors of survival in prostate cancer patients with bone metastasis and extremely high prostate-specific antigen levels. *Prostate Int.* **3**, 10-15, doi:10.1016/j.prnil.2015.02.006 (2015).
58. Bubendorf, L. *et al.* Metastatic patterns of prostate cancer: an autopsy study of 1,589 patients. *Hum Pathol* **31**, 578-583, doi: 10.1053/hp.2000.6698 (2000).
59. Bader, P., Burkhard, F. C., Markwalder, R. & Studer, U. E. Disease progression and survival of patients with positive lymph nodes after radical prostatectomy. Is there a chance of cure? *J. Urol.* **169**, 849-854, doi:10.1097/01.ju.0000049032.38743.c7 (2003).
60. Karantanos, T., Corn, P. G. & Thompson, T. C. Prostate cancer progression after androgen deprivation therapy: mechanisms of castrate resistance and novel therapeutic approaches. *Oncogene* **32**, 5501-5511, doi:10.1038/onc.2013.206 (2013).
61. Schroder, F. H. Progress in understanding androgen-independent prostate cancer (AIPC): a review of potential endocrine-mediated mechanisms. *Eur. Urol.* **53**, 1129-1137, doi:10.1016/j.eururo.2008.01.049 (2008).

62. Javidan, J., Deitch, A. D., Shi, X. B. & de Vere White, R. W. The androgen receptor and mechanisms for androgen independence in prostate cancer. *Cancer Invest.* **23**, 520-528, doi:U1878JK263348416 [pii] 10.1080/07357900500202721 (2005).

63. Zhu, M. L. *et al.* Tubulin-targeting chemotherapy impairs androgen receptor activity in prostate cancer. *Cancer Res.* **70**, 7992-8002, doi:10.1158/0008-5472.CAN-10-0585 (2010).
64. Paller, C. J. & Antonarakis, E. S. Cabazitaxel: a novel second-line treatment for metastatic castration-resistant prostate cancer. *Drug Des. Devel. Ther.* **5**, 117-124, doi:10.2147/DDDT.S13029 (2011).
65. Maestro, L. M. *et al.* Circulating tumor cells in solid tumor in metastatic and localized stages. *Anticancer Res.* **29**, 4839-4843, doi: http://ar.iiarjournals.org/content/29/11/4839.short (2009).
66. Pantel, K. & Alix-Panabieres, C. Circulating tumour cells in cancer patients: challenges and perspectives. *Trends Mol. Med.* **16**, 398-406, doi:10.1016/j.molmed.2010.07.001 (2010).
67. Alix-Panabieres, C. & Pantel, K. Challenges in circulating tumour cell research. *Nat. Rev. Cancer* **14**, 623-631, doi:10.1038/nrc3820 (2014).
68. Farreras, N. *et al.* Effect of early postoperative enteral immunonutrition on wound healing in patients undergoing surgery for gastric cancer. *Clin. Nutr.* **24**, 55-65, doi:10.1016/j.clnu.2004.07.002 (2005).
69. Almand, B. *et al.* Increased production of immature myeloid cells in cancer patients: a mechanism of immunosuppression in cancer. *J. Immunol.* **166**, 678-689 (2001).
70. Taylor, L. G., Canfield, S. E. & Du, X. L. Review of major adverse effects of androgen-deprivation therapy in men with prostate cancer. *Cancer* **115**, 2388-2399, doi:10.1002/cncr.24283 (2009).
71. Allison, D. D. & Grande-Allen, K. J. Review. Hyaluronan: a powerful tissue engineering tool. *Tissue Eng.* **12**, 2131-2140, doi:10.1089/ten.2006.12.2131 (2006).
72. Tezel, A. & Fredrickson, G. H. The science of hyaluronic acid dermal fillers. *Journal of cosmetic and laser therapy : official publication of the European Society for Laser Dermatology* **10**, 35-42, doi:10.1080/14764170701774901 (2008).
73. Fu, P., Jiang, X. & Arcasoy, M. O. Constitutively active erythropoietin receptor expression in breast cancer cells promotes cellular proliferation and migration through a MAP-kinase dependent pathway. *Biochem. Biophys. Res. Commun.* **379**, 696-701, doi:10.1016/j.bbrc.2008.12.146 (2009).
74. Ko, C. Y. *et al.* The use of chemokine-releasing tissue engineering scaffolds in a model of inflammatory response-mediated melanoma cancer metastasis. *Biomaterials* **33**, 876-885, doi:S0142-9612(11)01189-6 [pii] 10.1016/j.biomaterials.2011.10.002 (2012).

75. Nelson, M. T. *et al.* Preferential, enhanced breast cancer cell migration on biomimetic electrospun nanofiber 'cell highways'. *BMC Cancer* **14**, 825, doi:10.1186/1471-2407-14-825 (2014).
76. Xie, D. *et al.* Role of DAB2IP in modulating epithelial-to-mesenchymal transition and prostate cancer metastasis. *Proc. Natl. Acad. Sci. U S A* **107**, 2485-2490, doi:10.1073/pnas.0908133107 (2010).
77. Long, H. *et al.* Autocrine CCL5 signaling promotes invasion and migration of CD133+ ovarian cancer stem-like cells via NF-kappaB-mediated MMP-9 upregulation. *Stem Cells* **30**, 2309-2319, doi:10.1002/stem.1194 (2012).
78. Chen, H., Suo, K., Cheng, Y., Zheng, B. & Xu, L. Vascular endothelial growth factor C enhances cervical cancer migration and invasion via activation of focal adhesion kinase. *Gynecol. Endocrinol.* **29**, 20-24, doi:10.3109/09513590.2012.705387 (2013).
79. Mizutani, K. *et al.* The chemokine CCL2 increases prostate tumor growth and bone metastasis through macrophage and osteoclast recruitment. *Neoplasia* **11**, 1235-1242, doi:10.1593/neo.09988 (2009).

80. Giovarelli, M. *et al.* Tumor rejection and immune memory elicited by locally released LEC chemokine are associated with an impressive recruitment of APCs, lymphocytes, and granulocytes. *J. Immunol.* **164**, 3200-3206, doi: https://doi.org/10.4049/jimmunol.164.6.3200 (2000).
81. Kiefer, F. & Siekmann, A. F. The role of chemokines and their receptors in angiogenesis. *Cell Mol. Life Sci.* **68**, 2811-2830, doi:10.1007/s00018-011-0677-7 (2011).
82. Chaffer, C. L. & Weinberg, R. A. A perspective on cancer cell metastasis. *Science* **331**, 1559-1564, doi:10.1126/science.1203543 (2011).
83. Wan, L., Pantel, K. & Kang, Y. Tumor metastasis: moving new biological insights into the clinic. *Nat. Med.* **19**, 1450-1464, doi:10.1038/nm.3391 (2013).
84. Quail, D. F. & Joyce, J. A. Microenvironmental regulation of tumor progression and metastasis. *Nat. Med.* **19**, 1423-1437, doi:10.1038/nm.3394 (2013).
85. Taichman, R. S. *et al.* Use of the stromal cell-derived factor-1/CXCR4 pathway in prostate cancer metastasis to bone. *Cancer Res.* **62**, 1832-1837, doi: http://cancerres.aacrjournals.org/content/62/6/1832.full-text.pdf (2002).
86. Glogau, R. G. & Kane, M. A. Effect of injection techniques on the rate of local adverse events in patients implanted with nonanimal hyaluronic acid gel dermal fillers. *Dermatologic surgery : official publication for American Society for Dermatologic Surgery* **34 Suppl 1**, S105-109, doi:10.1111/j.1524-4725.2008.34251.x (2008).
87. Moreland, L. W. Intra-articular hyaluronan (hyaluronic acid) and hylans for the treatment of osteoarthritis: mechanisms of action. *Arthritis research & therapy* **5**, 54-67, doi: https://doi.org/10.1186/ar623 (2003).
88. Ahn, C. S. & Rao, B. K. The life cycles and biological end pathways of dermal fillers. *Journal of cosmetic dermatology* **13**, 212-223, doi:10.1111/jocd.12100 (2014).
89. Zhao, W., Jin, K., Li, J., Qiu, X. & Li, S. Delivery of stromal cell-derived factor 1alpha for in situ tissue regeneration. *Journal of biological engineering* **11**, 22, doi:10.1186/s13036-017-0058-3 (2017).
90. Fakhari, A. & Berkland, C. Applications and emerging trends of hyaluronic acid in tissue engineering, as a dermal filler and in osteoarthritis treatment. *Acta Biomater.* **9**, 7081-7092, doi:10.1016/j.actbio.2013.03.005 (2013).
91. Kabanov, A. V. & Vinogradov, S. V. Nanogels as Pharmaceutical Carriers: Finite Networks of Infinite Capabilities. *Angew. Chem. Int. Ed.* **48**, 5418-5429, doi: https://doi.org/10.1002/anie.200900441 (2009).
92. Gandaglia, G. *et al.* Impact of the Site of Metastases on Survival in Patients with Metastatic Prostate Cancer. *Eur. Urol.* **68**, 325-334, doi:10.1016/j.eururo.2014.07.020 (2015).
93. Kuru, B. *et al.* Prognostic factors for survival in breast cancer patients who developed distant metastasis subsequent to definitive surgery. *Singapore Med. J.* **49**, 904-911, doi: https://www.sma.org.sg/Publications/articles.aspx?ID=2517FA98-4510-4574-B8E2-482267EE2B95 (2008).
94. Xu, X., Jha, A. K., Duncan, R. L. & Jia, X. Heparin-decorated, hyaluronic acid-based hydrogel particles for the controlled release of bone morphogenetic protein 2. *Acta Biomater.* **7**, 3050-3059, doi:10.1016/j.actbio.2011.04.018 (2011).
95. Wang, W., Cameron, A. G. & Ke, S. Developing fluorescent hyaluronan analogs for hyaluronan studies. *Molecules* **17**, 1520-1534, doi:10.3390/molecules17021520 (2012).
96. Xu, X., Jha, A. K., Harrington, D. A., Farach-Carson, M. C. & Jia, X. Hyaluronic Acid-Based Hydrogels: from a Natural Polysaccharide to Complex Networks. *Soft Matter* **8**, 3280-3294, doi:10.1039/C2SM06463D (2012).
97. Jha, A. K. *et al.* Structural Analysis and Mechanical Characterization of Hyaluronic Acid-Based Doubly Cross-Linked Networks. *Macromolecules* **42**, 537-546, doi:10.1021/ma8019442 (2009).

98. Oh, J. K., Lee, D. I. & Park, J. M. Biopolymer-based microgels/nanogels for drug delivery applications. *Progress in Polymer Science* **34**, 1261-1282, doi: https://doi.org/10.1016/j.progpolymsci.2009.08.001 (2009).
99. Gaumet, M., Gurny, R. & Delie, F. Fluorescent biodegradable PLGA particles with narrow size distributions: preparation by means of selective centrifugation. *Int. J. Pharm.* **342**, 222-230, doi:10.1016/j.ijpharm.2007.05.001 (2007).
100. Dulong, V. *et al.* Hyaluronan-based hydrogels particles prepared by crosslinking with trisodium trimetaphosphate. Synthesis and characterization. *Carbohydrate Polymers* **57**, 1-6, doi: https://doi.org/10.1016/j.carbpol.2003.12.006 (2004).
101. Jha, A. K., Malik, M. S., Farach-Carson, M. C., Duncan, R. L. & Jia, X. Hierarchically structured, hyaluronic acid-based hydrogel matrices via the covalent integration of microgels into macroscopic networks. *Soft Matter* **6**, 5045-5055, doi:10.1039/C0SM00101E (2010).
102. Cai, T. *et al.* Novel thermogelling dispersions of polymer nanoparticles for controlled protein release. *Nanomedicine : nanotechnology, biology, and medicine* **8**, 1301-1308, doi:10.1016/j.nano.2012.02.002 (2012).
103. Blackburn, W. H., Dickerson, E. B., Smith, M. H., McDonald, J. F. & Lyon, L. A. Peptide-functionalized nanogels for targeted siRNA delivery. *Bioconjug. Chem.* **20**, 960-968, doi:10.1021/bc800547c (2009).
104. Baker, D. W. *et al.* Development of optical probes for in vivo imaging of polarized macrophages during foreign body reactions. *Acta Biomater.* **10**, 2945-2955, doi:10.1016/j.actbio.2014.04.001 (2014).
105. Zhou, J., Tsai, Y. T., Weng, H., Baker, D. W. & Tang, L. Real time monitoring of biomaterial-mediated inflammatory responses via macrophage-targeting NIR nanoprobes. *Biomaterials* **32**, 9383-9390, doi:10.1016/j.biomaterials.2011.08.064 (2011).
106. Thevenot, P. T. *et al.* The effect of incorporation of SDF-1alpha into PLGA scaffolds on stem cell recruitment and the inflammatory response. *Biomaterials* **31**, 3997-4008, doi:10.1016/j.biomaterials.2010.01.144 (2010).
107. Dupont, K. M. *et al.* Human stem cell delivery for treatment of large segmental bone defects. *Proc. Natl. Acad. Sci. U S A* **107**, 3305-3310, doi:10.1073/pnas.0905444107 (2010).
108. Sutton, E. J., Henning, T. D., Pichler, B. J., Bremer, C. & Daldrup-Link, H. E. Cell tracking with optical imaging. *Eur. Radiol.* **18**, 2021-2032, doi:10.1007/s00330-008-0984-z (2008).
109. Nair, A. *et al.* Biomaterial implants mediate autologous stem cell recruitment in mice. *Acta Biomater.* **7**, 3887-3895, doi:S1742-7061(11)00296-0 [pii] 10.1016/j.actbio.2011.06.050 (2011).
110. Siegel, R. L., Miller, K. D. & Jemal, A. Cancer statistics, 2019. *CA. Cancer J. Clin.* **69**, 7–34 (2019).
111. National Cancer Institute. Cancer Stat Facts: Esophageal Cancer. (2019). Available at: https://seer.cancer.gov/statfacts/html/esoph.html.
112. Gamboa, A. M. *et al.* Treatment allocation in patients with early-stage esophageal adenocarcinoma: Prevalence and predictors of lymph node involvement. *Cancer* **122**, 2150–2157 (2016).
113. Lowe, V. J. *et al.* Comparison of positron emission tomography, computed tomography, and endoscopic ultrasound in the initial staging of patients with esophageal cancer. *Mol. Imaging Biol.* **7**, 422–430 (2005).
114. Wang, W.-P., He, S.-L., Yang, Y.-S. & Chen, L.-Q. Strategies of nodal staging of the TNM system for esophageal cancer. *Ann. Transl. Med.* **6**, 77–77 (2018).
115. Holmes, R. S. & Vaughan, T. L. Epidemiology and Pathogenesis of Esophageal Cancer. *Semin. Radiat. Oncol.* **17**, 2–9 (2007).
116. Akutsu, Y. *et al.* The prevalence of overall and initial lymph node metastases in clinical t1n0 thoracic esophageal cancer: From the results of jcog0502, a prospective multicenter study. *Ann. Surg.* (2016). doi:10.1097/SLA.0000000000001557

117. Wang, Y., Zhu, L., Xia, W. & Wang, F. Anatomy of lymphatic drainage of the esophagus and lymph node metastasis of thoracic esophageal cancer. *Cancer Manag. Res.* **10**, 6295–6303 (2018).
118. Schiefer, A. I., Schoppmann, S. F. & Birner, P. Lymphovascular invasion of tumor cells in lymph node metastases has a negative impact on survival in esophageal cancer. *Surg. (United States)* **160**, 331–340 (2016).
119. Lieberman, M. D., Shriver, C. D., Bleckner, S. & Burt, M. Carcinoma of the esophagus: Prognostic significance of histologic type. *J. Thorac. Cardiovasc. Surg.* **109**, 130–139 (1995).
120. Akutsu, Y. & Matsubara, H. The significance of lymph node status as a prognostic factor for esophageal cancer. *Surg. Today* **41**, 1190–1195 (2011).
121. Cho, J. W. *et al.* Lymph Node Metastases in Esophageal Carcinoma: An Endoscopist's View. *Clin. Endosc.* **47**, 523 (2014).
122. Van Vliet, E. P. M., Heijenbrok-Kal, M. H., Hunink, M. G. M., Kuipers, E. J. & Siersema, P. D. Staging investigations for oesophageal cancer: A meta-analysis. *Br. J. Cancer* (2008). doi:10.1038/sj.bjc.6604200
123. Sakurada, A. *et al.* Diagnostic performance of diffusion-weighted magnetic resonance imaging in esophageal cancer. *Eur. Radiol.* **19**, 1461–1469 (2009).
124. Boone, J. *et al.* Sentinel node biopsy during thoracolaparoscopic esophagectomy for advanced esophageal cancer. *World J. Surg. Oncol.* (2016). doi:10.1186/s12957-016-0866-9
125. Van Den Eynden, G. G. *et al.* Distinguishing blood and lymph vessel invasion in breast cancer: A prospective immunohistochemical study. *Br. J. Cancer* (2006). doi:10.1038/sj.bjc.6603152
126. Driemel, C. *et al.* Context-dependent adaption of EpCAM expression in early systemic esophageal cancer. *Oncogene* **33**, 4904–4915 (2014).
127. Lin, H. K. *et al.* Portable filter-based microdevice for detection and characterization of circulating tumor cells. *Clin. Cancer Res.* (2010). doi:10.1158/1078-0432.CCR-10-1105
128. Tanaka, F. *et al.* Circulating tumor cell as a diagnostic marker in primary lung cancer. *Clin. Cancer Res.* (2009). doi:10.1158/1078-0432.CCR-09-1095
129. Hofman, V. *et al.* Detection of circulating tumor cells as a prognostic factor in patients undergoing radical surgery for non-small-cell lung carcinoma: Comparison of the efficacy of the CellSearch Assay™ and the isolation by size of epithelial tumor cell method. *Int. J. Cancer* (2011). doi:10.1002/ijc.25819
130. Dawood, S. *et al.* Circulating tumor cells in metastatic breast cancer: From prognostic stratification to modification of the staging system? *Cancer* (2008). doi:10.1002/cncr.23852
131. Gires, O. & Stoecklein, N. H. Dynamic EpCAM expression on circulating and disseminating tumor cells: Causes and consequences. *Cellular and Molecular Life Sciences* (2014). doi:10.1007/s00018-014-1693-1
132. den Toonder, J. Circulating tumor cells: the Grand Challenge. *Lab Chip* (2011). doi:10.1039/c0lc90100h
133. Butler, T. P. & Gullino, P. M. Quantitation of Cell Shedding Into Efferent Blood of Mammary Adenocarcinoma. *Cancer Res.* (1975).
134. Kang, Y. & Pantel, K. Tumor Cell Dissemination: Emerging Biological Insights from Animal Models and Cancer Patients. *Cancer Cell* (2013). doi:10.1016/j.ccr.2013.04.017
135. Kaifi, J. T. *et al.* Tumor-cell homing to lymph nodes and bone marrow and CXCR4 expression in esophageal cancer. *J. Natl. Cancer Inst.* (2005). doi:10.1093/jnci/dji431
136. Hosch, S. *et al.* Malignant potential and cytogenetic characteristics of occult disseminated tumor cells in esophageal cancer. *Cancer Res.* **60**, 6836–6840 (2000).
137. Tachezy, M. *et al.* ALCAM (CD166) expression and serum levels are markers for poor survival of esophageal cancer patients. *Int. J. Cancer* **131**, 396–405 (2012).
138. Stoecklein, N. H. *et al.* Direct Genetic Analysis of Single Disseminated Cancer Cells for Prediction of Outcome and Therapy Selection in Esophageal Cancer. *Cancer Cell* **13**, 441–453 (2008).
139. Hristozova, T. *et al.* The presence of circulating tumor cells (CTCs) correlates with lymph node

metastasis in nonresectable squamous cell carcinoma of the head and neck region (SCCHN). *Ann. Oncol.* (2011). doi:10.1093/annonc/mdr130
140. Reeh, M. *et al.* Circulating tumor cells as a biomarker for preoperative prognostic staging in patients with esophageal cancer. *Ann. Surg.* (2015). doi:10.1097/SLA.0000000000001130
141. Bobek, V. *et al.* Cultivation of circulating tumor cells in esophageal cancer. *Folia Histochem. Cytobiol.* (2014). doi:10.5603/FHC.2014.0020
142. Gros, S. J. *et al.* Involvement of CXCR4 Chemokine Receptor in Metastastic HER2-Positive Esophageal Cancer. *PLoS One* **7**, (2012).
143. Thorban, S. *et al.* Immunocytochemical detection of disseminated tumor cells in the bone marrow of patients with esophageal carcinoma. *J. Natl. Cancer Inst.* (1996). doi:10.1093/jnci/88.17.1222
144. Ko, C. Y. *et al.* The use of chemokine-releasing tissue engineering scaffolds in a model of inflammatory response-mediated melanoma cancer metastasis. *Biomaterials* (2012). doi:10.1016/j.biomaterials.2011.10.002
145. Wang, T. *et al.* Matched biopsy and resection specimens of gastric and gastroesophageal adenocarcinoma show high concordance in HER2 status. *Hum. Pathol.* **45**, 970–975 (2014).
146. Yan, M. *et al.* HER2 expression status in diverse cancers: review of results from 37,992 patients. *Cancer Metastasis Rev.* **34**, 157–164 (2015).
147. König, A. M. *et al.* Concordance of HER2 status in primary tumour and lymph nodemetastases in patients with esophageal carcinoma. *Anticancer Res.* **33**, 4975–4982 (2013).
148. Press, M. F. *et al.* HER2 Status in Advanced or Metastatic Gastric , Esophageal , or Gastroesophageal Adenocarcinoma for Entry to the TRIO-013 / LOGiC Trial of Lapatinib. **16**, 228–239 (2017).
149. Tan, C. *et al.* Potential biomarkers for esophageal cancer. *Springerplus* **5**, (2016).
150. Farace, F. *et al.* A direct comparison of CellSearch and ISET for circulating tumour-cell detection in patients with metastatic carcinomas. *Br. J. Cancer* **105**, 847–853 (2011).
151. Chen, W. *et al.* Nanoroughened Surfaces for Efficient Capture of Circulating Tumor Cells without Using Capture Antibodies. *ACS Nano* 566–575 (2012). doi:10.1021/nn304719q
152. Yano, S. *et al.* Efficacy of a cell-cycle decoying killer adenovirus on 3-D Gelfoam®-histoculture and tumor-sphere models of chemo-resistant stomach carcinomatosis visualized by FUCCI imaging. *PLoS One* **11**, 1–10 (2016).
153. Yano, S. *et al.* Cancer cells mimic in vivo spatial-temporal cell-cycle phase distribution and chemosensitivity in 3-dimensional gelfoam histoculture but not 2-dimensional culture as visualized with real-time fucci imaging. *Cell Cycle* **14**, 808–819 (2015).
154. Tome, Y. *et al.* 3-dimensional tissue is formed from cancer cells in vitro on gelfoam ®, but not on matrigelTM. *J. Cell. Biochem.* **115**, 1362–1367 (2014).
155. Rades, D., Golke, H., Schild, S. E. & Kilic, E. The Impact of Tumor Expression of Erythropoietin Receptors and Erythropoietin on Clinical Outcome of Esophageal Cancer Patients Treated With Chemoradiation. *Int. J. Radiat. Oncol. Biol. Phys.* **71**, 152–159 (2008).
156. Wei, Q. *et al.* EGFR, HER2 and HER3 expression in esophageal primary tumours and corresponding metastases. *Int. J. Oncol.* (2007).
157. Shimada, Y., Imamura, M., Wagata, T., Yamaguchi, N. & Tobe, T. Characterization of 21 newly established esophageal cancer cell lines. *Cancer* **69**, 277–284 (1992).
158. Diederich, S. Staging of oesophageal cancer. *Cancer Imaging* **2**, 75–80 (2007).
159. Thevenot, P. T. *et al.* The effect of incorporation of SDF-1α into PLGA scaffolds on stem cell recruitment and the inflammatory response. *Biomaterials* (2010). doi:10.1016/j.biomaterials.2010.01.144
160. Marshall, J. V. Cell Migration. *Encycl. Biol. Chem. Second Ed.* **769**, 430–435 (2013).
161. Sutton, E. J., Henning, T. D., Pichler, B. J., Bremer, C. & Daldrup-Link, H. E. Cell tracking with optical imaging. *European Radiology* (2008). doi:10.1007/s00330-008-0984-z
162. Lee, C. R., Grodzinsky, A. J. & Spector, M. The effects of cross-linking of collagen-glycosaminoglycan scaffolds on compressive stiffness , chondrocyte-mediated contraction ,

proliferation and biosynthesis. **22**, 3145–3154 (2001).
163. Baker, D. W. *et al.* Development of optical probes for in vivo imaging of polarized macrophages during foreign body reactions. *Acta Biomater.* **10**, 2945–2955 (2014).
164. Song, X. *et al.* A novel human-like collagen hydrogel scaffold with porous structure and sponge-like properties. *Polymers (Basel).* **9**, 1–16 (2017).
165. Cai, T. *et al.* Novel thermogelling dispersions of polymer nanoparticles for controlled protein release. *Nanomedicine Nanotechnology, Biol. Med.* (2012). doi:10.1016/j.nano.2012.02.002
166. Ohara, T. *et al.* The establishment of a new mouse model with orthotopic esophageal cancer showing the esophageal stricture. *Cancer Lett.* **293**, 207–212 (2010).
167. Loh, Q. L. & Choong, C. Three-Dimensional Scaffolds for Tissue Engineering Applications: Role of Porosity and Pore Size. *Tissue Eng. Part B Rev.* **19**, 485–502 (2013).
168. Murphy, C. M., Haugh, M. G. & O'Brien, F. J. The effect of mean pore size on cell attachment, proliferation and migration in collagen-glycosaminoglycan scaffolds for bone tissue engineering. *Biomaterials* **31**, 461–466 (2010).
169. Izbicki, J. R. *et al.* Prognostic Value of Immunohistochemically Identifiable Tumor Cells in Lymph Nodes of Patients with Completely Resected Esophageal Cancer. *N. Engl. J. Med.* **337**, 1188–1194 (1997).

Biography

Yi-Hui Huang's interests focus on the new diagnoses and the new treatment for the diseases. After receiving her bachelor's degree in chemical engineering from Yuan Ze University in 2004, she joined Life Science master program at Tamkang University. Studying the embryonic development of the zebrafish model inspired her to continue using this model to understand the mechanism of human polycystic kidney disease in Chang Gung memorial hospital after her graduation in 2007. For these years, she realized that the knowledge of fundamental research does not improve the current therapy. She joined Dr. Liping Tang's lab in the Bioengineering Department at UTA. Her studies focused on the new therapeutic and diagnostic strategy of osteoarthritis, cancer and implant-induced inflammatory response. As a Ph.D. student, she received the second place of graduate projects of innovation day 2018 in UTA as a co-author and published 12 papers. She will be working as a postdoctoral fellow in Dr. Tang's lab.

Academic degrees

UT Arlington, Arlington, USA (Jan 2014 – July 2019)
Degree: Doctoral degree
Major: Bioengineering

Tamkang University, Danshui, Taiwan (Sep 2005 – Jun 2007)
Degree: Master of Science
Major: Life Sciences

Yuan Ze University, Taoyuan, Taiwan (Sep 2000 – Jun 2004)
Degree: Bachelor of Science
Major: Chemical Engineering

Publications and Awards

A. Conferences:

[1] **Y. Huang**, A. Hakamivala, A. Nair, J.T. Hsieh, L. Tang "CCL-21 Releasing Cancer Trap for Capturing Metastatic Prostate" Cancer BMES 2017 Annual Meeting, 2017 Phoenix, Arizona, USA.

[2] M. Khang, J. Zhou, **Y. Huang,** A. Hakamivala, S. Li, L. Tang "Preparation of Injectable Thermogelling Nanoparticles for chemokine release and Cancer Cell Entrapment". 2019 Society For Biomaterials Annual Meeting & Exposition. 2019 Seattle, WA, USA.

[3] S. Li, J. Zhou, A. Hakamivala, **Y. Huang**, W. Cong, J. Borrelli, L. Tang "Treatment of Osteoarthritis Using Macrophage-Targeting Hyaluronic Acid Microscaffolds". Society for Biomaterials 2018 Annual Meeting & Exposition. 2018 Atlanta, Georgia, USA.

B. Publications:

[1] Y.H. Chen, **Y.H. Huang**, C.C. Wen, Y.H. Wang, W.L. Chen, L.C. Chen, H.J. Tsay, Movement disorder and neuromuscular change in zebrafish embryos after exposure to caffeine, Neurotoxicol Teratol 30(5) (2008) 440-7.

[2] J. Wu, Q. Ding, A. Dutta, Y. Wang, **Y.H. Huang**, H. Weng, L. Tang, Y. Hong, An injectable extracellular matrix derived hydrogel for meniscus repair and regeneration, Acta Biomater 16 (2015) 49-59.

[3] M.Y. Chang, J.K. Lu, Y.C. Tian, Y.C. Chen, C.C. Hung, **Y.H. Huang**, Y.H. Chen, M.S. Wu, C.W. Yang, Y.C. Cheng, Inhibition of the P2X7 receptor reduces cystogenesis in PKD, J Am Soc Nephrol 22(9) (2011) 1696-706.

[4] C. Xu, **Y. Huang**, J. Wu, L. Tang, Y. Hong, Triggerable Degradation of Polyurethanes for Tissue Engineering Applications, ACS Appl Mater Interfaces 7(36) (2015) 20377-88.

[5] C. Xu, **Y. Huang**, L. Tang, Y. Hong, Low-Initial-Modulus Biodegradable Polyurethane Elastomers for Soft Tissue Regeneration, ACS Appl Mater Interfaces 9(3) (2017) 2169-2180.

[6] C. Xu, **Y. Huang**, G. Yepez, Z. Wei, F. Liu, A. Bugarin, L. Tang, Y. Hong, Development of dopant-free conductive bioelastomers, Sci Rep 6 (2016) 34451.

[7] M.M. Good, T.I. Montoya, H. Shi, J. Zhou, **Y. Huang**, L. Tang, J.F. Acevedo, R.A. Word, Thermosensitive hydrogels deliver bioactive protein to the vaginal wall, PLoS One 12(10) (2017) e0186268.

[8] J. Zhou, H. Weng, **Y. Huang**, Y. Gu, L. Tang, W. Hu, Ratiometric Reactive Oxygen Species Nanoprobe for Noninvasive In Vivo Imaging of Subcutaneous Inflammation/Infection, J Biomed Nanotechnol 12(8) (2016) 1679-87.

[9] **Y. Huang**, J. Zhou, A. Hakamivala, J. Wu, Y. Hong, J. Borrelli, L. Tang, An optical probe for detecting chondrocyte apoptosis in response to mechanical injury, Sci Rep 7(1) (2017) 10906.

[10] V. Kearney, **Y. Huang**, W. Mao, B. Yuan, L. Tang, Canny edge-based deformable image registration, Phys Med Biol 62(3) (2017) 966-985.

[11] M.C. Phipps, **Y. Huang**, R. Yamaguchi, N. Kamiya, N.S. Adapala, L. Tang, H.K. Kim, In vivo monitoring of activated macrophages and neutrophils in response to ischemic osteonecrosis in a mouse model, J Orthop Res 34(2) (2016) 307-13.

[12] S. Li, W. Cong, A. Hakamivala, **Y. Huang**, J. Borrelli, Jr., L. Tang, Hyaluronic Acid-Based Optical Probe for the Diagnosis of Human Osteoarthritic Cartilage, Nanotheranostics 2(4) (2018) 347-359.

[13] M.K. Khang, J. Zhou, **Y. Huang**, A. Hakamivala, L. Tang, Preparation of a novel injectable in situ -gelling nanoparticle with applications in controlled protein release and cancer cell entrapment, RCS Advances 8(60) (2018) 34625-34633.

[14] H. Vu, J. Zhou, **Y. Huang**, A. Hakamivala, M.K. Khang, L. Tang, Development of a dual-wavelength fluorescent nanoprobe for in vivo and in vitro cell tracking consecutively, Bioorganic & Medicinal Chemistry In press. (2019).

C. List of Awards:

Selected as the second place of graduate projects of innovation day 2018, Sponsored by Dean of Engineering, the University of Texas at Arlington, April 2018.

D. Scholarships:

Spring 2014 – Spring 2019 Graduate Research Assistantship
Fall 2014 – Spring 2019 STEM Doctoral Fellowship